Electronic and atomic structure of Co/Ge nanoislands on the Ge(111) surface

D. A. Muzychenko,[1,*] K. Schouteden,[2,†] and C. Van Haesendonck[2]
[1]*Faculty of Physics, M.V. Lomonosov Moscow State University, 119991 Moscow, Russia*
[2]*Laboratory of Solid-State Physics and Magnetism, KU Leuven, BE-3001 Leuven, Belgium*
(Received 27 June 2013; revised manuscript received 8 October 2013; published 27 November 2013)

We report on a detailed investigation of the electronic and atomic structure of nanometer-size Co/Ge islands obtained by solid-state reactive deposition of Co atoms on a Ge(111)$c(2\times 8)$ surface. Relying on scanning tunneling microscopy (STM) and spectroscopy (STS) measurements combined with density functional theory based calculations, the atomic structure of the Co/Ge(111)$\sqrt{13}\times\sqrt{13}\,R13.9^\circ$ surface reconstruction is determined. Real-space STM imaging combined with Fourier-transform analysis reveals the coexistence of two inequivalent phases of $\sqrt{13}\times\sqrt{13}\,R13.9^\circ$ reconstructed Co/Ge nanoislands that are rotated by $+13.9^\circ$ and -13.9° with respect to the $[2\bar{1}\bar{1}]$ direction. STS spectra probe a small band gap that varies within the $\sqrt{13}\times\sqrt{13}\,R13.9^\circ$ surface unit cell between 10 and 250 meV, suggesting local metallic behavior. According to the proposed atomic-structure model, each Co/Ge(111)$\sqrt{13}\times\sqrt{13}\,R13.9^\circ$ surface unit cell contains one Ge adatom and six Co atoms that are located at *hollow sites* below the top surface Ge layer and that are stacked in the form of an equilateral triangle. The Ge adatom is located asymmetrically with respect to the Co triangle and occupies two different, yet physically equivalent, positions, giving rise to two chiral phases of Co/Ge nanoislands. The Co/Ge valence band is dominated by Co atom derived 3*d* states, while states in the conduction band stem from Ge adatom and Ge rest-atom derived states. Analysis of the bonding properties confirms the stability of the proposed Co/Ge atomic structure and reveals significant charge transfer from Co atoms to Ge rest atoms, suggesting ionic or metallic-covalent interaction.

DOI: 10.1103/PhysRevB.88.195436 PACS number(s): 68.35.−p, 68.47.Fg, 68.37.Ef, 73.20.At

I. INTRODUCTION

Advances in nanoelectronics during the last decade stem to a large extent from the undiminished efforts of the scientific community to overcome the difficulties encountered in the miniaturization of electronic devices. Currently, the downscaling of the conventional Si-based metal-oxide-semiconductor (field-effect) transistors[1] is reaching its intrinsic limits.[2] In order to proceed beyond these limits, new devices, that are able to add novel functionalities to Si-based transistors, need to be developed. Moreover, the use of new materials with electronic properties superior to those of Si is required. For this purpose, Ge offers yet unexploited opportunities[3–5] because of its higher electron and hole mobility[6] and its compatibility with the Si-based technologies. On the other hand, nanostructured materials that combine a high spin polarization with semiconducting properties, such as diluted magnetic semiconductors[7,8] and ferromagnet/semiconductor hybrids,[9,10] are considered as highly promising candidates for future spintronic devices[11,12] and quantum logic gates[13–15] that rely on controlled manipulation of the charge and the spin of electrons.

In this view, an atomistic understanding of the growth of 3*d* transition metals on semiconductor surfaces is of utmost importance because the resulting electronic and spin properties crucially depend on the precise atomic configurations. The growth of ferromagnetic materials (Fe, Co, Ni, etc.) on Ge leads to the formation of complex germanide compounds at the ferromagnet/semiconductor interface.[16–18] The phase evolution of, e.g., Co and Ni germanides as a function of the formation temperatures[19–21] and their Schottky diode behavior[22–25] have already been studied intensively. Furthermore, it has been demonstrated that various metal germanides (NiGe, PdGe, $PtGe_x$, and $CoGe_2$) also offer perspectives for use as self-aligned contact materials in Ge-based devices because of their low electrical resistance, low formation temperature, and high thermal stability.[26,27] Due to the reactive nature of 3*d* ferromagnetic metals, reconstruction of the surface atoms upon deposition can occur even at room temperature.[28] The growth of ferromagnetic materials on Ge can therefore not be described by standard epitaxial growth models such as the Volmer-Weber or the Frank–van der Merwe models. Thin-film germanide reactions are typically considered to be similar to silicide reactions. However, when compared to Si, the growth process of ferromagnetic materials on Ge surfaces has received considerably less attention.

The (111) surface of Ge is of particular interest because of the various metal-induced reconstructions that may occur upon annealing of the surface. Several experimental studies have already been devoted to the growth and electronic properties of Mn_xGe_y (Refs. 10 and 29–31) and Ag (Refs. 32–36) on Ge(111)$c(2\times 8)$ surfaces. Mn-doped Ge is considered as a promising diluted magnetic semiconductor, while the Ag-induced $\sqrt{3}\times\sqrt{3}\,R30^\circ$ surface reconstruction (hereafter referred to as the $\sqrt{3}R30$ reconstruction)[37–40] can be used as an effective buffer layer that is suitable for growth of thin ferromagnetic (FM) layers.[41,42] Direct growth of FM layers on the Ge surface yields complex germanide phases that form a nonmagnetic layer at the interface [e.g., for Co layers with thickness below 3 monolayers (MLs) (Refs. 42 and 43)], which is detrimental for electron spin injection from the ferromagnet to the semiconductor.

Previous studies of the growth of Co on Ag/Ge(111)$\sqrt{3}R30$ revealed the formation of two-dimensional (2D) islands that exhibit two different surface reconstructions: Some islands exhibit a $\sqrt{13}\times\sqrt{13}\,R13.9^\circ$ (hereafter referred to as $\sqrt{13}R14^\circ$) reconstruction, while other islands have a $(\sqrt{3}\times\sqrt{3})$ reconstruction.[44] The ratio between the

probabilities of appearance for both types of islands has been found to depend on the Co coverage and on the annealing temperature.[45–47] However, the precise formation process of the complex Co/Ag/Ge(111) reconstruction and the role played by the Ag buffer layer is not fully understood.[48] A supporting theoretical model for the atomic and electronic structure of the $\sqrt{13}R14^\circ$ reconstruction still needs to be developed. Unambiguous interpretation of the reported experimental results for the Co/Ag/Ge(111) system obviously requires detailed understanding of the more simple growth process of Co on bare Ge(111) surfaces. Experimental and theoretical atomic-scale studies of the initial stages of Co adsorption on bare Ge(111) surfaces are, however, still lacking.

Here, we report on our combined study based on scanning tunneling microscopy (STM) and scanning tunneling spectroscopy (STS) and on *ab initio* calculations of the $\sqrt{13}R14^\circ$ reconstructed Co/Ge(111) surface that is obtained by solid-state reactive deposition of Co on the Ge(111)$c(2 \times 8)$ surface and subsequent annealing. By real-space STM imaging as well as Fourier-transform analysis we reveal the existence of two structurally inequivalent types of $\sqrt{13}R14^\circ$ reconstructed nanometer-size Co/Ge islands having a different chirality. Relying on voltage-dependent STM imaging, we identified the two surface unit cells (SUCs) of the $\sqrt{13}R14^\circ$ reconstruction and determined an atomic-scale model of the reconstructed surface. This is verified in detail by direct comparison with density functional theory (DFT) based simulations of STM images. Each SUC consists of six Co atoms that are located at *hollow sites* below the top surface layer and that are arranged in the form of an equilateral triangle, and of one Ge adatom that is located above a Ge atom of the second layer. The Ge adatom is located asymmetrically with respect to the "Co triangle" and can occupy two different yet physically equivalent sites, yielding two different chiral phases for the Co/Ge $\sqrt{13}R14^\circ$ nanoislands. By means of STS we show that the Co/Ge $\sqrt{13}R14^\circ$ nanoislands exhibit metallic behavior with a vanishing band gap that locally varies within the $\sqrt{13}R14^\circ$ SUC, yielding opportunities for use as Ohmic contact material.[26] We find that filled-states STM images are dominated by Co atom derived states, while the empty states mainly originate from the Ge adatoms and from the group of Ge rest atoms. Analysis of the electronic structure and bonding properties confirms the stability of the proposed Co/Ge atomic structure. Moreover, our analysis reveals a remarkable charge transfer from the Co atoms to the Ge rest atoms as well as nearest-neighbor interactions between Co-Ge atomic species that point towards the existence of ionic or metallic-covalent bonding.

II. EXPERIMENTAL METHODS

STM and STS measurements are performed with a low-temperature ultrahigh vacuum (UHV, base pressure is about 4×10^{-12} mbar) STM setup (Omicron Nanotechnology) at 4.5 K using W tips. The tips are cleaned *in situ* by repeated flashing well above 1500 °C in order to remove the surface oxide layer and additional contamination. The tip quality is routinely checked by acquiring atomic-resolution images of the "herringbone" reconstruction of the Au(111) surface.[49,50] STM topography imaging is performed in constant current mode. STS spectra are recorded in the current imaging tunneling spectroscopy (CITS) mode with a grid size of 200×200 current-voltage $I(V)$ spectra. Everywhere in the text the tunneling bias voltage V_t refers to the sample voltage, while the STM tip is virtually grounded. Image processing is done by Nanotec WSxM.[51]

Ge samples are doped with P at a doping level of $n_P \sim 10^{18}$ cm^{-3}, resulting in n-type bulk conductivity with resistivity $\rho_{\text{bulk}} \sim 0.01\ \Omega$ cm. Ge slabs with dimensions $4 \times 1.5 \times 0.8$ mm^3 and with their long axis aligned along the (111) direction are cleaved[52] *in situ* at room temperature in the UHV preparation chamber (base pressure is about 5×10^{-11} mbar) of the STM setup. After cleavage, the samples are heated to 400 °C for a few minutes to transform the Ge(111)2×1 surface into the $c(2 \times 8)$ reconstructed Ge(111) surface. Next, Co atoms are deposited at a rate of 0.004 ± 0.001 monolayers (MLs) per second from a high-purity Co rod by means of electron-beam evaporation. During deposition, the Ge substrate is kept at 100 °C. We take 1 ML coverage equal to 7.22×10^{14} atoms/cm^2, i.e., the atomic density of the unreconstructed Ge(111) surface. After Co deposition, the sample is annealed to 300 °C–350 °C for about 10 min.

III. EXPERIMENTAL RESULTS

A. Growth of $\sqrt{13} \times \sqrt{13}\,R13.9^\circ$ reconstructed Co/Ge(111) nanoislands

In Fig. 1, we present (a) a typical large-scale and (b) a closeup view STM topography image of the Ge(111) surface after deposition of about $\frac{1}{4}$ ML of Co as described above. It can be seen in Fig. 1 that 2D islands with nanometer size

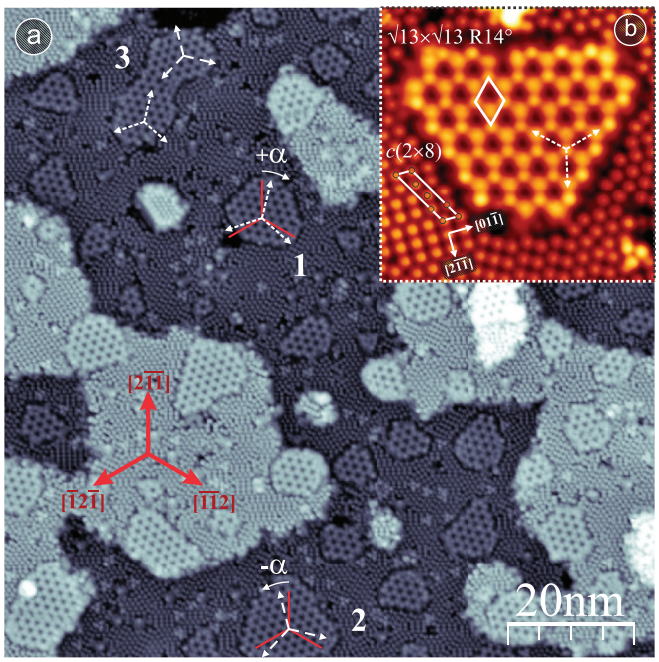

FIG. 1. (Color online) (a) 100×100 nm^2 and (b) 14×14 nm^2 STM topography images ($V_t = +2.0$ V, $I_t = 50$ pA) of the Co/Ge(111) surface. The $\sqrt{13} \times \sqrt{13}\,R13.9^\circ$ and $c(2 \times 8)$ surface unit cell are indicated by the white solid rhombus and parallelogram, respectively, in (b). Other symbols are explained in the text.

and with $\sqrt{13}R14^\circ$ surface reconstruction (discussed in more detail in the next section) are formed, which are referred to as Co/Ge nanoislands hereafter. The Co/Ge nanoislands have lateral sizes ranging from a few nanometers up to 50 nm and are randomly distributed across the Ge(111) surface. In the high-resolution empty-states STM image of a Co/Ge nanoisland in Fig. 1(b) the $\sqrt{13}R14^\circ$ reconstructed nanoisland appears to have a similar height as the surrounding Ge(111) surface. We find that the precise height depends on the tunneling voltage V_t. For example, the height of a nanoisland with respect to the surrounding Ge(111) surface is $h \simeq 10$ pm (peak to peak) at $V_t = +2.0$ V and $h \simeq 38$ pm at $V_t = +1.5$ V. Based on an analysis of 10 140 × 140 nm^2 STM topography images, the total area covered by the Co/Ge nanoislands is found to be 23% ± 7%.

Parts of Figs. 1(a) and 1(b) also reveal that the initial long-range $c(2 \times 8)$ reconstruction of the Ge(111) surface surrounding the Co/Ge nanoislands is slightly modified due to the Co deposition. The Ge surface atoms now exhibit local (2×2) and $c(2 \times 4)$ reconstructions that reflect the intrinsic $c(2 \times 8)$ reconstruction. Within the Chadi and Chiang model,[53] the $c(2 \times 8)$ unit cell is constructed out of a (2×2) and a $c(2 \times 4)$ subunit cell with two types of adatoms and rest atoms on top of the Ge(111) with different local environments.[54–61] The surface unit cells (SUCs) of the $c(2 \times 8)$ and $\sqrt{13}R14^\circ$ reconstruction are indicated in Fig. 1(b). Because of the threefold rotational symmetry of the Ge(111) surface, the $[01\bar{1}]$, $[1\bar{1}0]$, and $[\bar{1}01]$ surface crystallographic directions (rotated by 120° with respect to each other) can be inferred from STM topography images for the initial $c(2 \times 8)$ reconstruction as well as for the local (2×2) and $c(2 \times 4)$ reconstructed regions. This also allows us to determine the projections of the bulk $[2\bar{1}\bar{1}]$, $[\bar{1}\bar{1}2]$, and $[\bar{1}2\bar{1}]$ crystallographic directions on the Ge(111) surface [indicated by red solid arrows in Fig. 1(a)].

Upon more careful inspection of Fig. 1(a) it can be seen that the $\sqrt{13}R14^\circ$ reconstruction of the Co/Ge nanoislands is rotated by an angle α of about $+14^\circ$ or -14° with respect to the $[2\bar{1}\bar{1}]$ direction. This is illustrated in Fig. 1(a) by the white dotted arrows and the white dashed arrows for the islands labeled 1 and 2, respectively. The long diagonal of the $\sqrt{13}R14^\circ$ SUC rhombus for nanoisland 1 is rotated clockwise with respect to the $[2\bar{1}\bar{1}]$ direction (hereafter referred to as the $RIGHT\sqrt{13}$) orientation, while for nanoisland 2 the long diagonal is rotated anticlockwise (hereafter referred to as the $LEFT\sqrt{13}$ orientation). Both orientations appear with the same probability. Exceptionally, nanoislands can be found that exhibit both $RIGHT\sqrt{13}$ and $LEFT\sqrt{13}$ orientations [see island labeled 3 in Fig. 1(a)]. It can hence be expected that at full coverage the surface will consist of Co/Ge$\sqrt{13}R14^\circ$ domains with the two different orientations that are separated by domain boundaries.

B. Fourier-transform analysis

We investigated the Co/Ge nanoislands and their $\sqrt{13}R14^\circ$ reconstruction in more detail via Fourier-transform (FT) analysis of the STM topography images. In Fig. 2(a), we present the 2D FT image of the $RIGHT\sqrt{13}$ Co/Ge nanoisland which was already presented in Fig. 1(b). The (2×2) and $c(2 \times 4)$ reconstructed regions of the surrounding Ge surface

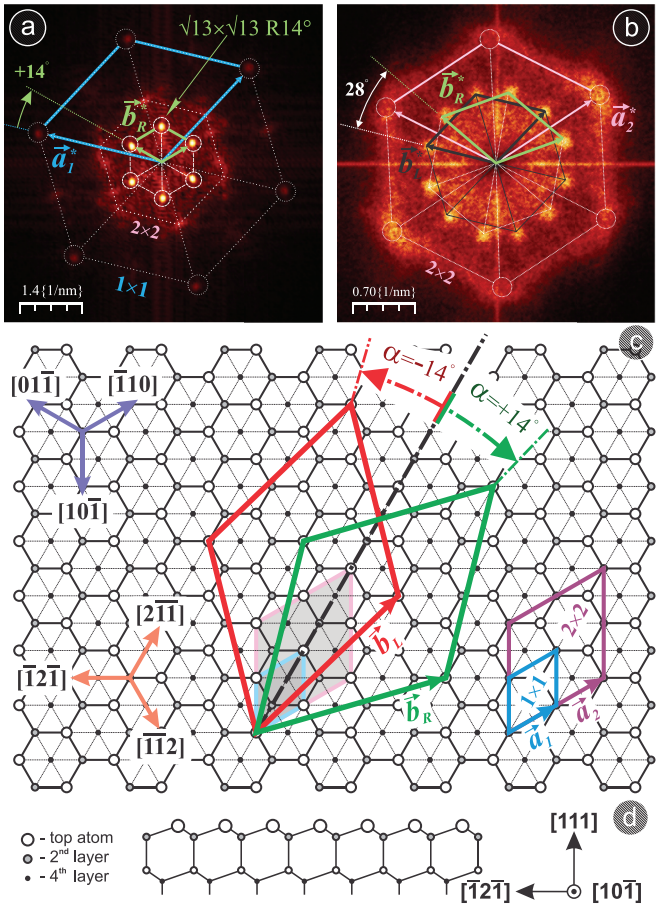

FIG. 2. (Color online) (a) 2D FT image of Fig. 1(b). The Bragg spots indicated by the reciprocal lattice vectors $\vec{a}_1^*$ stem from the (1×1) unreconstructed Ge(111) surface, while the spots indicated by the reciprocal lattice vectors $\vec{b}_R^*$ originate from the $RIGHT\sqrt{13}$ reconstructed Co/Ge nanoislands. (b) 2D FT image of Fig. 1(a). The vectors $\vec{a}_2^*$ stem from the (2×2) unreconstructed Ge(111) surface, while the vectors $\vec{b}_R^*$ and $\vec{b}_L^*$ are linked to the $RIGHT\sqrt{13}$ and $LEFT\sqrt{13}$ reconstructed Co/Ge nanoislands, respectively. (c), (d) Schematic top and side views, respectively, of the atomic structure of the unreconstructed Ge(111) surface. The main crystallographic directions and high-symmetry atom sites are indicated.

and the threefold rotational symmetry of the Ge(111) surface give rise to the six outer Bragg spots in Fig. 2(a). These spots correspond to the reciprocal lattice vector set with the length $|\vec{a}_1^*| = 1.774$ Å^{-1} $(2\pi/|\vec{a}_1^*| = 3.54$ Å) of the unreconstructed Ge(111)(1 × 1) atomic lattice. The six inner Bragg spots [the reciprocal lattice vector set $|\vec{b}_R^*| = 0.455$ Å^{-1} $(2\pi/|\vec{b}_R^*| = 13.8$ Å)] stem from the surface reconstruction of the $RIGHT\sqrt{13}$ type Co/Ge nanoisland. The sizes of the vector sets are related as $|\vec{a}_1^*| = \sqrt{13}\,|\vec{b}_R^*|$ and the sets are rotated clockwise over an angle $\alpha = +13.2^\circ \pm 1.6^\circ$ with respect to each other. The latter value matches well with the angle derived directly from the STM topography image (see previous section).

Figure 2(b) presents the 2D FT image of the STM topography image in Fig. 1(a). In this case, the Bragg spots corresponding to $\vec{a}_1^*$ can not be observed due to the larger size of the STM image, while the Bragg spots stemming from the

2×2 surface reconstruction, i.e., $|\vec{a}_2^*| = 2|\vec{a}_1^*| = 0.868$ Å^{-1} ($2\pi/|\vec{a}_2^*| = 7.23$ Å) can still be discerned [they are also visible in Fig. 2(b)]. Note that the reciprocal vectors $\vec{a}_1^*$ and $\vec{a}_2^*$ are not rotated with respect to each other, implying they both can be used as an orientational reference for other spots. The 12 inner Bragg spots in Fig. 2(b) originate from the presence of Co/Ge nanoislands with both the $RIGHT\sqrt{13}$ and $LEFT\sqrt{13}$ reconstruction in Fig. 1(a). These spots can hence be interpreted in terms of the presence of two subsets of six spots with reciprocal vectors $\vec{b}_R^*$ and $\vec{b}_L^*$ of equal length and with a relative angle of $2\alpha = 29° \pm 2°$. The latter value is in a good agreement with the theoretical value of 27.8° for the $\sqrt{13}R14°$ reconstruction. The similar intensity of the two subsets of Bragg spots confirms that the $RIGHT\sqrt{13}$ and $LEFT\sqrt{13}$ Co/Ge nanoislands appear with the same probability in the STM images.

The fact that two types of $\sqrt{13}R14°$ Co/Ge nanoislands are formed on the Ge(111) surface can be understood by considering the atomic-scale model of the Ge(111) surface. Figures 2(c) and 2(d) present a sketch of the four surface layers of the unreconstructed Ge(111) surface. The (1×1) and (2×2) SUCs with (real-space) lattice vectors $\vec{a}_1$ and $\vec{a}_2$ are indicated in Fig. 2(c). When selecting a SUC, the origin of the vector $\vec{a}_1$ can be (arbitrarily) placed on one of the three different Ge atom sites: On the *top atom*, in front of the *second-layer atom* or in front of the *fourth-layer atom* (hereafter referred to as the *hollow site*) [see Figs. 2(c) and 2(d)]. The long diagonal of the SUC rhombus can be chosen along the $[2\bar{1}\bar{1}]$, $[\bar{1}\bar{1}2]$, or $[\bar{1}2\bar{1}]$ direction. This way, the complete Ge surface can be constructed by repeating the chosen SUC. For a given (1×1) SUC, there are two equivalent possibilities for the "adsorbate SUC" of the $\sqrt{13}R14°$ reconstruction, as indicated in Fig. 2(c). These SUCs have real-space lattice vectors with the length $|\vec{b}_R| = \sqrt{13}\,|\vec{a}_1|$ (green) and $|\vec{b}_L| = \sqrt{13}\,|\vec{a}_1|$ (red) vectors and are rotated over an angle of $+13.9°$ and $-13.9°$ with respect to the (1×1) SUC. Both SUCs are primitive $\sqrt{13}R14°$ unit cells, i.e., they are the simplest unit cells that are able to describe the $\sqrt{13}R14°$ structure. The experimentally observed $RIGHT\sqrt{13}$ and $LEFT\sqrt{13}$ orientations of the reconstructed Co/Ge nanoislands in Fig. 1(a) can hence be linked to these two different $\sqrt{13}R14°$ SUCs.

C. Inequivalence of the $RIGHT\sqrt{13}$ and $LEFT\sqrt{13}$ SUCs

Although the two SUCs that describe the $\sqrt{13}R14°$ reconstruction appear very similar, they are not fully equivalent. This becomes clear when considering the atomic structure of the unreconstructed Ge(111) surface that "supports" the $RIGHT\sqrt{13}$ and $LEFT\sqrt{13}$ SUCs in Fig. 2(c). It can be seen in Fig. 3 that the atomic arrangements within both SUCs is different, i.e., the SUCs exhibit mirror symmetry with respect to each other. The SUCs can hence not be transformed into each other by a simple rotation operation, but only by a mirror reflection with respect to the symmetry line indicated in Fig. 3. It is expected that this "inequivalence" of both types of reconstructed Co/Ge nanoislands gives rise to a different appearance of the islands in STM experiments. Indeed, while both types of Co/Ge nanoislands appear very similar in the empty-states regime [threefold rotational symmetry, see Fig. 1(a)], a mirror

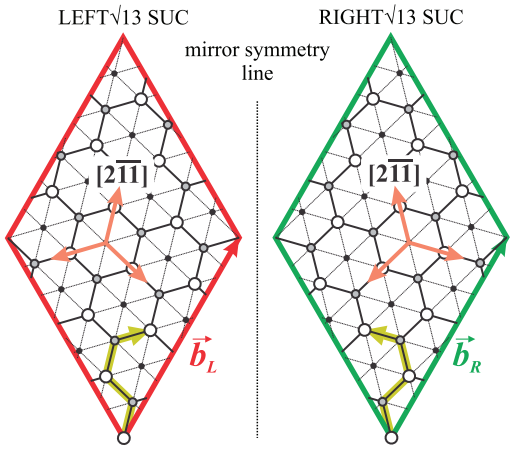

FIG. 3. (Color online) (Left) and (right) Schematic top view of the unreconstructed Ge(111) surface area that is "covered" by the $LEFT\sqrt{13}$ and $RIGHT\sqrt{13}$ SUCs of the $\sqrt{13}R14°$ surface reconstruction in Fig. 2(c), respectively. The arrangement of the Ge(111) surface atoms within the $LEFT\sqrt{13}$ and $RIGHT\sqrt{13}$ SUCs exhibits mirror symmetry with respect to each other (see the sequence of atoms indicated by the yellow arrows at the bottom of each SUC).

symmetry between the two types can be observed in the filled-states regime. Figures 4(a) and 4(c) present empty-states STM topography images of a $RIGHT\sqrt{13}$ and $LEFT\sqrt{13}$ Co/Ge nanoisland, respectively. The SUC is added for each image, together with an "orientational guide" that indicates the higher (brighter) and lower (darker) region of the $\sqrt{13}R14°$ SUC by a red and blue triangle, respectively. Figures 4(b) and 4(d) present filled-states STM topography images of the same areas presented in Figs. 4(a) and 4(c), respectively.

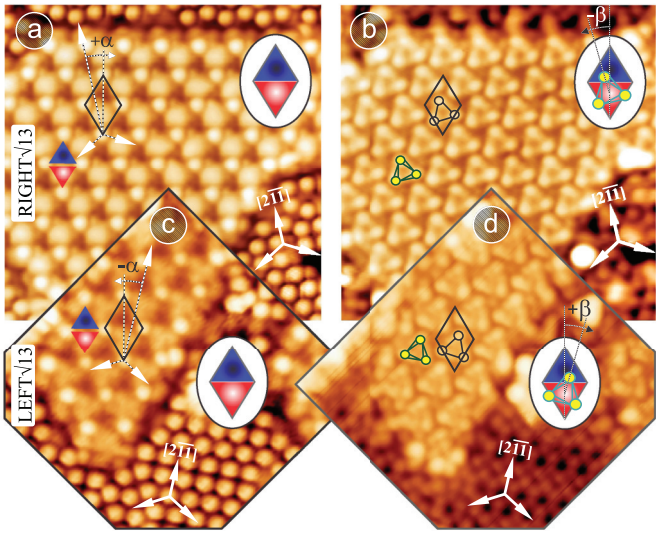

FIG. 4. (Color online) (a), (c) Empty-states ($V_t = +1.5$ V, $I_t = 150$ pA) and (b), (d) filled-states ($V_t = -1.5$ V, $I_t = 50$ pA) STM topography images of a $RIGHT\sqrt{13}$ and $LEFT\sqrt{13}$ reconstructed Co/Ge nanoisland. Image sizes are 15×15 nm^2 for (a), (b) and 10×10 nm^2 for (c), (d). The $\sqrt{13} \times \sqrt{13}\,R13.9°$ SUC is indicated by the black rhombus. An "orientational guide" is added to each of the images (see text for more details).

Determination of the SUCs for the empty- and filled-states regimes is discussed in more detail in Sec. III D.

In the filled-states regime [Figs. 4(b) and 4(d)], the $\sqrt{13}R14^\circ$ surface reconstruction of the Co/Ge nanoislands is observed as densely packed equilateral triangles with less bright edges and brighter spots at their corners, as previously also reported by Lin *et al.*[62] This is indicated in Figs. 4(b) and 4(d) by the added "orientational guide." One can see that the $RIGHT\sqrt{13}$ and $LEFT\sqrt{13}$ Co/Ge nanoislands exhibit mirror symmetry with respect to each other (along the vertical axis). The angle β between the long diagonal of the rhombus and the median of the equilateral triangle [see Figs. 4(b) and 4(d)] is about $\pm 14^\circ$, similar to what was found from our 2D FT analysis (see Sec. III B) and $\sqrt{13}R14^\circ$ SUCs modeling (Sec. IV). A simple analysis learns that $\beta = 0$ with respect to the crystallographic directions $[2\bar{1}\bar{1}]$. In other words, we can conclude that the bright triangles in the filled-states regime have the same orientation for the $RIGHT\sqrt{13}$ or $LEFT\sqrt{13}$ reconstructed Co/Ge nanoislands and that the three bright corners of the triangle indicate the $[2\bar{1}\bar{1}]$, $[\bar{1}\bar{1}2]$, and $[\bar{1}2\bar{1}]$ crystallographic directions.

It is important to note that the combination of filled-states and empty-states STM topography imaging allows us to unambiguously determine the phase of the $\sqrt{13}R14^\circ$ surface reconstruction of the Co/Ge nanoislands, without any further analysis of the orientation of the surrounding nanoislands and without determining the crystallographic directions of the surrounding Ge(111)$c(2 \times 8)$ surface (see Sec. III A). Moreover, from analysis of the $\sqrt{13}R14^\circ$ filled-states STM topography images, it is possible to determine the $[2\bar{1}\bar{1}]$, $[\bar{1}\bar{1}2]$, and $[\bar{1}2\bar{1}]$ crystallographic directions of the Ge(111) substrate.

D. Voltage-dependent STM investigation of the Co/Ge $\sqrt{13}R14^\circ$ surface reconstruction

High-resolution voltage-dependent STM imaging of Co/Ge nanoislands reveals structural details that have not yet been reported in previous STM-based studies.[44,45,62,63] Figure 5 presents a series of empty-states [(a1)–(a5)] and filled-states [(b1)–(b5)] STM topography images of the $\sqrt{13}R14^\circ$ surface reconstruction of a $RIGHT\sqrt{13}$ Co/Ge nanoisland, recorded at the same location and with the same STM tip for tunneling voltages V_t ranging from $+2.0$ to -1.5 V.

In order to exclude possible (thermal) drift effects of the piezo scanner during our voltage-dependent STM imaging, we record "dual-bias STM images." In particular, a different tunneling voltage is used for the *forward* and *backward* line scans that govern the *forward* and *backward* STM topography images. In Fig. 5, we also take into account the small (scan-speed-dependent) shift of about 0.2 Å that was found to exist between both recorded images with respect to each other and hence always use the same scan speed. The tunneling voltage for the forward image is fixed at $V_t = 2.00$ V and is used as a reference for the backward image for which the tunneling voltage is varied. This way, the dual-bias STM imaging allows us to compare exactly the same locations of the $\sqrt{13}R14^\circ$ SUC at different tunneling voltages. The $\sqrt{13}R14^\circ$ SUC, indicated by the dotted rhombus in Fig. 5, has a periodicity of $\sqrt{13} \times \sqrt{13}$ and a side length of 1.46 ± 0.04 nm.

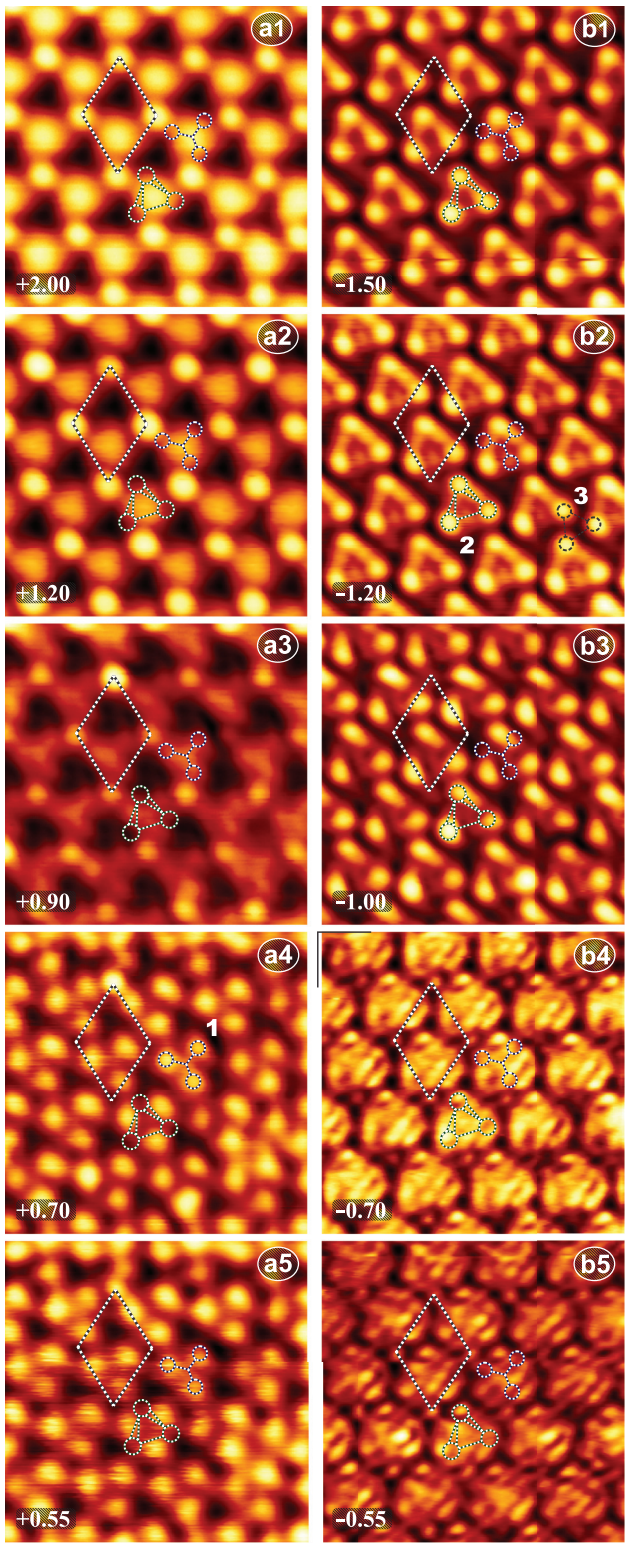

FIG. 5. (Color online) (a1)–(a5) Empty-states and (b1)–(b5) filled-states STM topography images of the Co/Ge $\sqrt{13} \times \sqrt{13}\,R13.9^\circ$ reconstruction on the Ge(111) surface. Image sizes are 6.3×6.3 nm^2. The tunneling voltage V_t is indicated for each image.

In the empty-states regime, at voltages above 1.0 V [Figs. 5(a1) and 5(a2)], topography is dominated by bright

spherical protrusions that are located at the four corners of the SUC rhombus, i.e., there exists one such protrusion for each SUC. These protrusions appear most pronounced in the 1.2 to 1.5 V tunneling voltage range [see Fig. 5(a2)]. In addition to the protrusions, a less bright feature can be observed in the lower half part of the SUC. This feature becomes more pronounced with increasing tunneling voltage, and around $V_t = 2.0$ V its brightness is similar to that of the protrusions at the rhombus corners. Both the protrusions at the corners and the extra feature in the lower half of the SUC become less clear with decreasing tunneling voltage below 1.0 V [Fig. 5(a3)], and around 0.8 V the feature in the lower half part of the SUC transforms into a structure consisting of three small bright spots that form an equilateral triangle [Figs. 5(a4) and 5(a5)]. The protrusions at the rhombus corners are no longer visible at these voltages. In Fig. 5(a4), the equilateral triangle is marked by the dotted symbol labeled 1. This triangle is duplicated at exactly the same location in all of the STM topography images in Fig. 5.

In the filled-states regime, at high voltages below −1.0 V [Figs. 5(b1)–5(b3)], the topography is dominated by equilateral triangles with less bright edges and brighter corners, similar to the STM topography images in Figs. 4(b) and 4(d). As already mentioned in Sec. III C, the angle between the median of the triangle and the long diagonal of the SUC rhombus is about −14°, i.e., the Co/Ge nanoisland is of type $RIGHT\sqrt{13}$. The triangular structure is indicated by a dotted symbol labeled 2 in Fig. 5(b2). This triangular symbol is duplicated at the same location in all of the STM topography images in Fig. 5. Note that this triangular feature 2 does not fit completely inside the SUC, i.e., the lower two bright spots lie somewhat outside the SUC. However, it can be seen that one SUC contains (in total) one triangular feature labeled 2. In particular, it can be seen that the three bright spots, which are indicated in an alternative way by label 3 in Fig. 5(b2), fit completely within a single SUC of the $\sqrt{13}R14°$ periodic structure. In the following, we prefer to use the structure labeled 2, as it is more consistent with the atomic-structure model we propose below. Above −1.0 V [Figs. 5(b4) and 5(b5)], the triangular structure 2 becomes less clear and the bright corners fade away. Instead, a fine structure appears within the contours of triangle 2 as well as small spots at the corners of the SUC rhombus. The voltage-dependent STM images allow us to develop and verify our atomic-structure model for the Co/Ge(111)$\sqrt{13}R14°$ surface reconstruction (see Sec. IV).

E. Electronic structure of Ge(111)$c(2 \times 8)$ and $\sqrt{13}R14°$ Co/Ge nanoislands

The surface electronic structure of bare Ge(111)$c(2 \times 8)$ has already been investigated in great detail using various experimental techniques, including angle-resolved photoemission spectroscopy (ARPES), inverse photoemission spectroscopy (IPES), and STS, as well as by *ab initio* calculations. In Fig. 6, we schematically illustrate the main contributions of electronic states to the surface density of states (SDOS) of the Ge(111)$c(2 \times 8)$ surface that have been reported in literature. Germanium is a semiconductor with a (relatively) large band gap E_g of about 0.74 eV at low temperature,

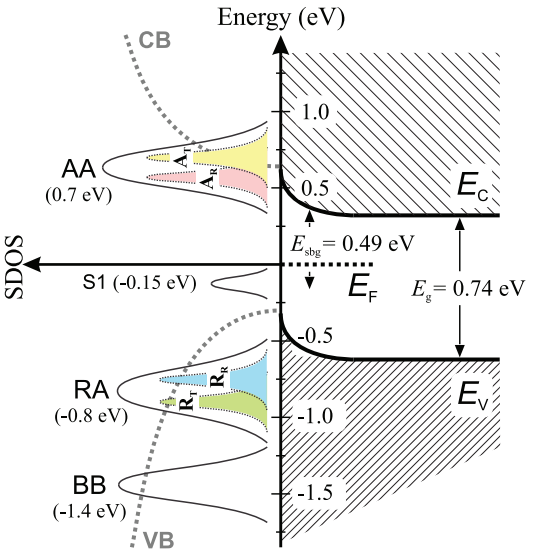

FIG. 6. (Color online) Energy scheme of the main contributions of electronic states to the Ge(111)$c(2 \times 8)$ surface density of states following reported ARPES, IPES, STS, and theoretical studies.

allowing clear observation of the Ge(111)$c(2 \times 8)$ surface band gap $E_{sbg} = 0.49 \pm 0.03$ eV.[64] The surface states are mainly localized at adatoms (AAs, emtpy-surface states) and rest atoms (RAs, filled-surface states). ARPES studies have revealed that the rest-atom derived states are located near −0.8 eV below the Fermi level E_F,[65–68] in good agreement with STS experiments[55,57,60] and *ab initio* calculations.[58,61,64] The deeper-lying state in the valence band near −1.4 eV below E_F is related to back-bond (BB) states of the adatoms and has been observed in ARPES experiments.[68] A contribution from these BB states to rest atoms has been reported as well.[58,61] Finally, STS[55,57,60] and IPES[69] measurements as well as theoretical studies[58,64] showed that the feature near 0.7 eV above E_F originates from adatom related states. The electronic properties of the Ge(111)$c(2 \times 8)$ surface states are, however, not yet fully understood. In particular, the origin of some aspects of the surface band structure related to the existence of two inequivalent "types" of adatoms (A_T, A_R) and rest atoms (R_T, R_R) (Ref. 58) that have a different Ge environment is still a matter of debate. Razado-Colambo *et al.* found that this inequivalence gives rise to a splitting of the rest-atom band and adatom band of about 0.1–0.2 eV (see Fig. 6) and a partial electron transfer from adatoms to rest atoms.[61] In addition, photoemission data by Aarts *et al.* revealed the existence of a surface band S1 around −0.15 eV below E_F that has a dangling-bond-like character and a (1 × 1) periodicity.[68] This could not be explained within the existing Ge(111)$c(2 \times 8)$ model and was related to partially filled adatom dangling bonds. However, recently, it has been shown that the S1 band is actually a combination of a band originating from states below adatom and rest-atom layers near the center of the Brillouin zone, while the outer part of the S1 band stems from rest-atom related states only.[61]

The electronic behavior of surface states typically drastically changes upon the adsorption of metal atoms. We therefore performed STS measurements to investigate the local electronic structure of the bare Ge(111)$c(2 \times 8)$ surface before

Co deposition as well as of the Co/Ge $\sqrt{13}R14^\circ$ surface reconstruction and the surrounding uncovered parts of the Ge surface. In order to take into account the effects of the different tunneling barrier for different tunneling voltages, we rely on the normalized differential conductance $(dI/dV)/(I/V)$, which is proportional to the local density of states (LDOS) of the surface, rather than on the differential conductance dI/dV. $(dI/dV)/(I/V)$ is obtained numerically from the recorded $I(V)$ spectra. However, division by the voltage Vleads to an artificial divergence around zero bias in the $(dI/dV)/(I/V)$ spectra. To eliminate the divergence around zero bias, we applied (limited) broadening to the (I/V) data values.[70] In Fig. 7(c), we present typical $(dI/dV)/(I/V)$ spectra recorded at (1) the bare Ge(111)$c(2\times 8)$ surface prior to Co atom deposition (black solid line), (2) the Ge(111) surface in-between the Co/Ge nanoislands after Co atom deposition (green dashed line), and (3) a $\sqrt{13}R14^\circ$ reconstructed Co/Ge nanoisland (red dashed-dotted line). The Fermi level E_F is located at 0 V. The spectra are obtained by

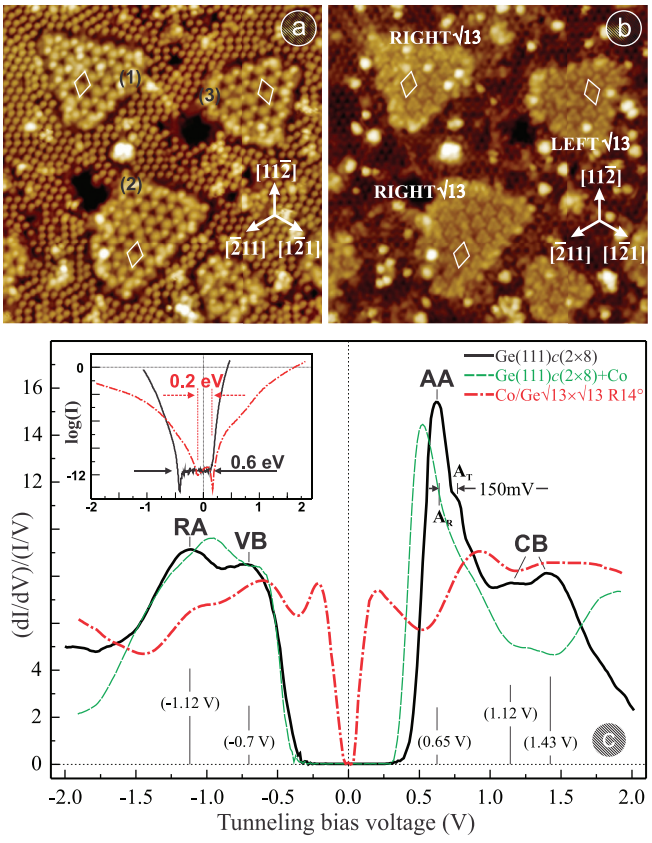

FIG. 7. (Color online) (a) Empty-states and (b) filled-states STM topography images ($V_t = +1.0$ V, $I_t = 20$ pA) of the same $RIGHT\sqrt{13}$ and $LEFT\sqrt{13}$ reconstructed Co/Ge nanoislands on the Ge(111) surface. (c) $(dI/dV)/(I/V)$ spectra taken at the Ge(111)$c(2\times 8)$ surface prior to Co atom deposition (black solid curve) and after Co deposition, i.e., at the $\sqrt{13}R14^\circ$ reconstructed Co/Ge nanoislands (red dashed-dotted curve) and at the defect-free areas with local $c(2\times 4)$ and (2×2) reconstructions in-between the Co/Ge nanoislands (green dashed curve). Inset: logarithm of $I(V)$ spectra taken on Ge(111)$c(2\times 8)$ (black solid curve) and on $\sqrt{13}R14^\circ$ reconstructed Co/Ge nanoislands (red dashed-dotted curve).

taking the numerical derivative of area-averaged $I(V)$ spectra (including typically 10^3–10^4 spectra) extracted from a CITS measurement. Figures 7(a) and 7(b) are empty-states and filled-states STM topography images, respectively, of the same Ge surface with $\sqrt{13}R14^\circ$ nanoislands, on which also the CITS data were recorded. Spectrum (2) in Fig. 7(c) is obtained by averaging CITS $I(V)$ data of defect-free areas with local $c(2\times 4)$ and (2×2) reconstructions that exist in-between the Co/Ge nanoislands, while spectrum (3) in Fig. 7(c) is obtained by averaging CITS data recorded at the three Co/Ge $\sqrt{13}R14^\circ$ nanoislands that are included in Figs. 7(a) and 7(b). Finally, spectrum (1) in Fig. 7(c) is obtained from another CITS measurement on bare defect-free Ge(111)$c(2\times 8)$ before Co atom deposition [topography image not included in Figs. 7(a) and 7(b)].

The spectrum of the bare Ge(111)$c(2\times 8)$ surface reveals several pronounced features that can be linked to the states presented in Fig. 6. The large peak near 0.65 V (labeled AA) can be attributed to the adatom related empty-surface-states band. Moreover, it can be seen that this peak exhibits a "shoulder" at its right-hand side, which points towards the existence of two inequivalent types of adatoms, as already discussed above. The splitting is found to be about 150 mV [measured in-between A_R and A_T, see Fig. 7(c)], in agreement with previous theoretical predictions.[58,61] Features in the spectrum at voltages above the adatom peak can be associated with conduction band (CB) states and a higher-lying surface-states band.[60] The two CB peaks at 1.12 and 1.43 V appear at significantly lower voltages (i.e., about 0.3 V closer to E_F) than the two CB peaks previously reported for p-type Ge(111)$c(2\times 8)$.[60] Similarly, the valence band (VB) peak in the filled-states regime near -0.7 V appears at about 0.3 V lower voltage. These shifts can be explained by the fact that the Fermi level E_F is closer to the CB for n-type material than for p-type material. Finally, in the filled-states regime, one can observe another (broad) peak at -1.12 V below E_F, which can be associated with the surface rest-atom band (labeled RA). In contrast to the case of the adatom related peak, we do not resolve a spectral shoulder that can be linked to two different types of rest atoms. This can be explained by the fact that the rest-atom band is rather close to the VB peak, which hampers resolving the R_T and R_R peaks. It should be noted that the rest-atom peak in the STS spectra appears at significantly lower energies when compared to earlier ARPES spectra.[68] It has recently been shown that the voltage at which the rest-atom peak appears strongly depends on the tunneling current and on the temperature. This has been related to disorder-induced states stemming from (disordered) adatoms that appear at domain boundaries of the Ge(111)$c(2\times 8)$ surface, resulting in a nonequilibrium source of positive charge.[60]

In order to determine the width and the energy positions of the edges of the surface band gap, we plot the logarithm of the (absolute value of the) tunneling current as a function of tunneling voltage [see inset of Fig. 7(c)]. This way, the energy band gap is observed as the (noisy) flat (zero-slope) region around $V = 0$. For the bare Ge(111)$c(2\times 8)$ surface (black solid line), the band gap is located in-between the bulk VB states (below E_F) and the surface adatom derived states (above E_F). The surface band gap ranges from about -0.45 to 0.15 V and the band gap width is 0.60 eV.

In Fig. 7(c), the STS spectrum of the $\sqrt{13}R14^\circ$ reconstructed Co/Ge nanoislands (red dashed-dotted line) differs significantly from that of the bare Ge(111)$c(2\times 8)$ surface (black solid line) as well as from that of the local $c(2\times 4)$ and (2×2) reconstructed Ge(111) surface (green dashed line). It can be seen that the tunneling spectra of the Ge(111) surface before and after Co atom deposition are rather similar, although the STM topography images of both surfaces appear to be quite different. There occurs only a small shift of the RA and AA peaks of about 0.1–0.2 V towards E_F, while the width of the surface band gap remains almost the same. On the other hand, the $\sqrt{13}R14^\circ$ reconstructed Co/Ge nanoislands exhibit a strongly reduced surface band gap when compared to the surrounding Ge surface. To minimize the (potential) influence of nonequilibrium effects in the tunneling spectra, we relied on low-current STS measurements and used identical tunneling voltage and current set-point values for the acquisition of $I(V)$ curves on bare Ge(111)$c(2\times 8)$ and on Co/Ge $\sqrt{13}R14^\circ$ reconstructed nanoislands. From the logarithm of the $I(V)$ spectrum taken on a Co/Ge nanoisland [red dashed-dotted line in the inset of Fig. 7(c)], a band gap of 0.2 eV can be inferred. The Fermi level E_F is located symmetrically in the surface band gap determined by the two surface-states related peaks located at -0.2 and 0.2 V. Furthermore, we note that careful comparison of the electronic structure of the two $RIGHT\sqrt{13}$ reconstructed Co/Ge nanoislands labeled (1) and (2) in Figs. 7(a) and 7(b) reveals no significant differences in the STS spectra. Remarkably, also no significant differences are observed between $RIGHT\sqrt{13}$ reconstructed Co/Ge nanoislands (1,2) and $LEFT\sqrt{13}$ reconstructed Co/Ge nanoislands (3), both in local (non-area-averaged) STS $(dI/dV)/(I/V)$ spectra taken at different sites within the $\sqrt{13}R14^\circ$ SUC of different Co/Ge nanoislands, and in area-averaged STS spectra such as those presented in Fig. 7(c). We therefore conclude that the $RIGHT\sqrt{13}$ and $LEFT\sqrt{13}$ reconstructed Co/Ge nanoislands exhibit an identical electronic structure. Finally, we want to note that in the low-current STS measurement we did not observe any significant dependence of the $(dI/dV)/(I/V)$ spectra on the tunneling current for the Co/Ge $\sqrt{13}R14^\circ$ reconstructed nanoislands.

In Fig. 8, we present $(dI/dV)/(I/V)$ spectra recorded at three inequivalent locations within the $\sqrt{13}R14^\circ$ SUC indicated in the inset: (1) an *adatom site*, (2) a "*central*" *site*, and (3) a "*depressed*" *site*. The spectra are the average of 30 to 50 individual spectra recorded at the same locations (1), (2), and (3), but on different Co/Ge nanoislands. It can be seen that the surface band gap depends on the exact location within the $\sqrt{13}R14^\circ$ SUC and varies from below 0.01 eV (i.e., close to metallic behavior) at location (3), up to about 0.24 eV at location (1). The band gaps of the *adatom site* (1) and of the *central sites* (2) are slightly asymmetric with respect to the Fermi level and are enclosed in-between the two surface-states related bands located near -0.25 V (S_{1F}) and 0.2 V (S_{1E}). The S_{1E} peak appears closer to E_F at the *central site* and the *depressed site*, while S_{1F} always appears at the same energy. Another pronounced peak S_{2E} is observed around 0.8 V at the *adatom site* and around 0.9 V at the *central site*, i.e., around the same energy at which AA states are found on bare Ge(111)$c(2\times 8)$ surfaces [see Fig. 7(c)]. At the *depressed site*, the S_{2E} state is only weakly visible. Instead, an additional state

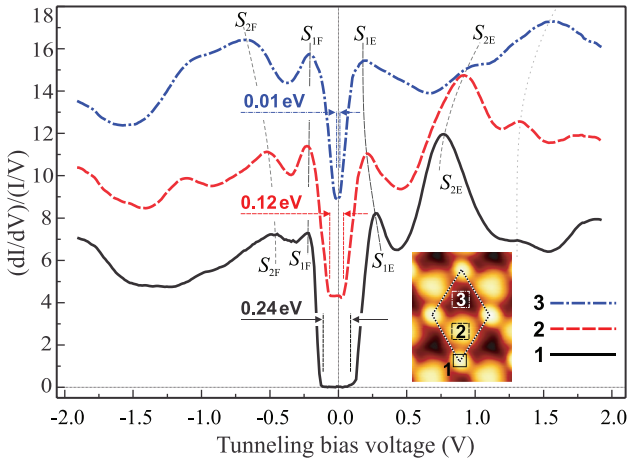

FIG. 8. (Color online) Normalized differential conductance spectra taken at the three different locations within the $\sqrt{13}R14^\circ$ SUC that are indicated in the STM topography image in the inset ($V_t = +1.8$ V, $I_t = 20$ pA). Curves are shifted vertically for clarity.

S_{3E} can be observed around 1.6 V. Finally, in the filled-states regime an additional surface-states peak S_{2F} is found to exist at the three locations (1), (2), and (3), shifting from -0.5 V at the *adatom site* to -0.7 V at the *depressed site*.

In Fig. 9, we present a series of 2D maps of the tunneling differential conductance $dI/dV(x,y,V)$, which is proportional to the LDOS, derived from a CITS measurement at the same locations as those used for Figs. 7(a) and 7(b). This way, the existence of the low-energy surface states in the Co/Ge $\sqrt{13}R14^\circ$ nanoislands can be visualized using the LDOS maps. One can see that the LDOS near the Fermi level is higher on the nanoislands when compared to the surrounding area, in both the empty-states [Fig. 9(a1)] and filled-states regimes [Fig. 9(b1)]. This is consistent with our STS-based observation of a very small surface band gap at the *depressed sites* of the $\sqrt{13}R14^\circ$ reconstruction (see Fig. 8), i.e., there is an almost metallic conductivity. At voltages below 100 mV the main contribution to the LDOS of the nanoislands stems from the tails of the S_{1E} and S_{1F} surface states. At higher voltages, the LDOS at the *adatom sites* and the *central sites* increases and the Co/Ge nanoislands can be clearly discerned in the LDOS maps up to $V = 0.6$ V and down to $V = -0.7$ V for the empty and filled states, respectively. At more elevated voltages, the VB and AA states start to contribute to the LDOS. In the voltage range between 0.6 and 1.2 V, the LDOS maps reveal pronounced patterns on the $\sqrt{13}R14^\circ$ reconstructed Co/Ge nanoislands [Figs. 9(a2) and 9(a3)]. This can be linked to the S_{2E} surface state that exists within this voltage range (see Fig. 8). Around 0.7–0.8 V, the S_{2E} state is mainly localized at the *adatom site*, and for $V = 0.9$–1.0 V it also appears at the *central site*. Furthermore, a large amount of surface defects can be resolved on the surrounding Ge surface in-between the nanoislands. This may be related to a (random) embedding of a fraction of the deposited Co atoms into the Ge(111) surface, which may in turn give rise to the observed breaking of the (initial) long-range $c(2\times 8)$ surface reconstruction. From our careful comparison of the LDOS maps of $RIGHT\sqrt{13}$ and $LEFT\sqrt{13}$ reconstructed Co/Ge nanoislands for a wide range of energies, we can conclude that

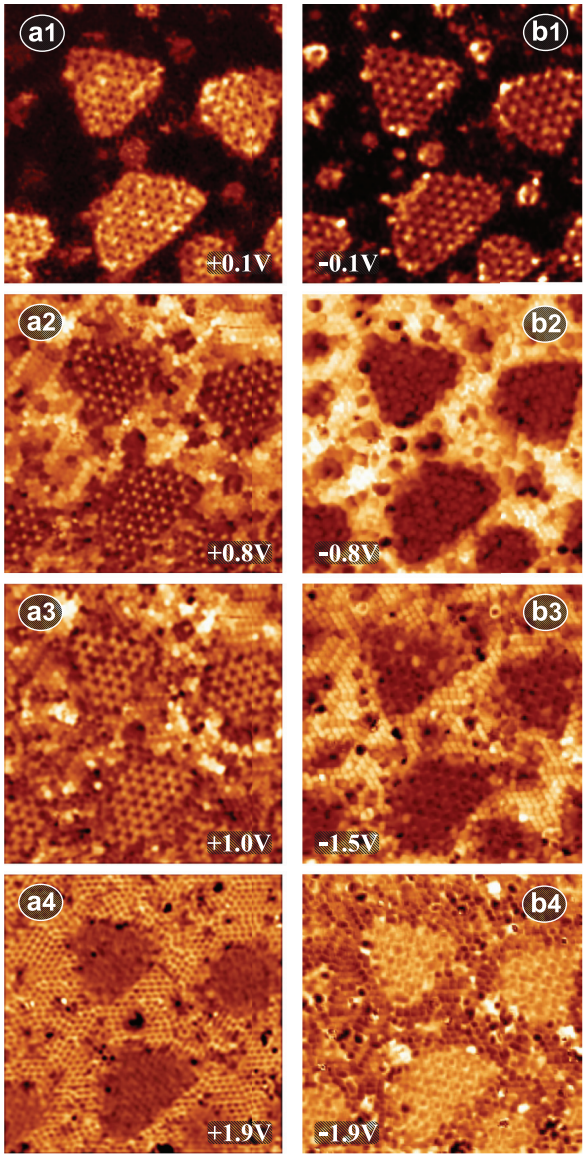

FIG. 9. (Color online) Filled-states (a1–a4) and empty-states (b1–b4) CITS derived LDOS maps at the same location as in Figs. 7(a) and 7(b) (the tunneling voltage V_t is indicated for each image).

the $RIGHT\sqrt{13}$ and $LEFT\sqrt{13}$ reconstructions exhibit, in spite of their different appearance in STM topography images, identical local electronic properties.

IV. COMPUTATIONAL METHODS AND STRUCTURAL MODEL

A. Details of the calculations

Our theoretical investigation of the Co-induced $\sqrt{13}\times\sqrt{13}\,R13.9^\circ$ surface reconstruction of the Ge(111) surface is performed using DFT based calculations[71,72] within the Perdew-Burke-Ernzerhof[73] (PBE) generalized gradient approximation[74] (GGA) exchange-correlation energy functional. Calculations are performed using the SIESTA code,[75,76] which relies on the expansion of the Kohn-Sham orbitals using a linear combination of pseudoatomic orbitals. The core electrons are implicitly treated by using norm-conserving Troullier-Martins pseudopotentials[77] with the following electronic configuration of the elements: H = $1s^1$, Ge = (Ar $3d^{10}$) $4s^2\,4p^2$, and Co = (Ar) $4s^2\,3d^7$, where the core configurations are indicated between parentheses. A mesh cutoff of 300 Ry for the grid integration and a split double-zeta basis set without spin polarization are used in all calculations. Integrals over the Brillouin zone are summed on a $6\times6\times1$ Monkhorst-Pack mesh,[78] ensuring convergence of the self-consistent field iteration process until the changes of total energy are below 0.1 meV.

Our calculations are performed in three stages. First, we start from an unreconstructed Ge(111) slab with $\sqrt{13}R14^\circ$ surface periodicity. Second, an (arbitrary) amount of so-called "foreign" Co and Ge atoms is added at different locations (based on symmetry considerations) above the Ge(111) surface and the equilibrium configurations of the Co/Ge system are determined using conjugate gradient (CG) geometry optimization. Third, the electronic structure of a $n\times n$ supercell is calculated and used for the DFT based simulations of STM topography images. The second and third steps are repeated until the best match between the experimental and simulated STM images is achieved.

In order to model the Ge(111) unreconstructed surface with $\sqrt{13}R14^\circ$ periodic boundary conditions, an extended monoclinic unit cell with basis vector lengths $|\vec{x}| = a_0\sqrt{13}/\sqrt{2}$, $|\vec{y}| = a_0\sqrt{13}/\sqrt{2}$, and $|\vec{z}| = a_0\,4\sqrt{3}$ is used (see Fig. 10), where $a_0 = 5.641$ Å is the optimized bulk Ge lattice constant for the selected DFT approximation. The angle between the $\vec{x} = \vec{b}_R$ and $\vec{y} = \vec{b}_R$ vectors is 60° and for the $RIGHT\sqrt{13}$ SUC both vectors are rotated over an angle of +13.9° with respect to the vector $\vec{a}_1$ [i.e., the projection of the bulk lattice vector on the (111) surface, see Fig. 2(c)]. The unit cell consists of a slab of 10 Ge atomic layers [see Fig. 10(b)] of which one atomic layer is saturated by hydrogen atoms, yielding 130 Ge atoms and 13 H atoms per unit cell. The vacuum space above the Ge surface is 21.7 Å. Since the bare Ge(111)$c(2\times8)$ surface reconstructs from the $c(2\times8)$ to the $\sqrt{13}R14^\circ$ reconstruction during the annealing after Co atom deposition, we can not simply estimate the initial amount of Ge adatoms and rest atoms within the new $\sqrt{13}R14^\circ$ SUC. First, the amount of Ge adatoms and rest atoms in the SUC is reduced and becomes fractional upon transition from the old SUC to the new one because of the different size S of the SUCs for both reconstructions, i.e., $S_{c(2\times8)}/S_{\sqrt{13}} = \frac{16}{13}$. Second, during the reconstruction, the Co atoms may "push away" the Ge adatoms that are initially present below the Co/Ge nanoislands. Therefore, we start our modeling from the bare unreconstructed and unrelaxed Ge(111) surface.

Next, Co and Ge atoms are added on top of the (111) surface as illustrated in Fig. 10. The amount of added atoms and their adsorption sites are chosen based on symmetry considerations related to the lattice symmetry of the $RIGHT\sqrt{13}$ SUC and on STM images for the filled-states and empty-states regimes (see discussion in Sec. III D). Here, we focus as an example on the $RIGHT\sqrt{13}$ atomic structure, but detailed complementary results were also obtained for the $LEFT\sqrt{13}$ atomic structure. During the CG geometry optimization, the atoms of the six topmost Ge layers are allowed to relax, while

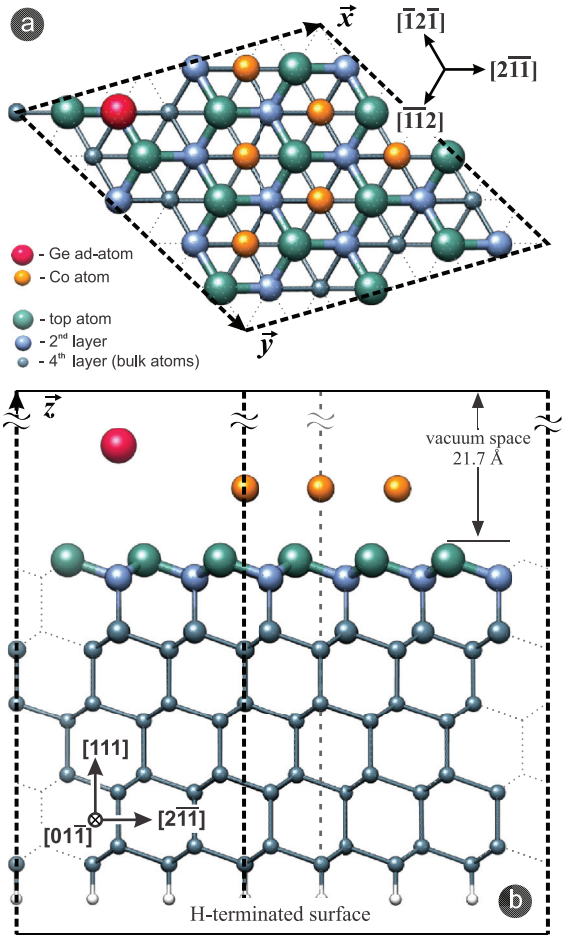

FIG. 10. (Color online) (a) Top and (b) side views of the ball-and-stick model of the unreconstructed Ge(111) slab for the $\sqrt{13}R14^\circ$ SUC. The model contains 10 Ge layers with vacuum space above the upper surface layer and a H-terminated bottom surface layer. The $\sqrt{13}R14^\circ$ unit cell is indicated by bold black dashed lines. The atoms of the first and second Ge layers are presented as the larger green and blue spheres, respectively, while atoms below the third layer are indicated by the smaller gray-green spheres. The red and yellow spheres indicate the initial (prior to CG geometry optimization) adsorption positions of one Ge adatom (red sphere) and six Co atoms (yellow spheres), respectively.

the positions of the atoms of the four lower-lying Ge layers and of the H layer are frozen. The "foreign" atoms and the slab atoms are allowed to relax until all atomic forces acting on the released atoms are smaller than 5 meV/Å and the remaining numerical error in the total energy is smaller than 10^{-4} eV for each optimization step. Each optimized structure is subjected to an annealing simulation. The annealing allows the system to surmount energy barriers and hence can give rise to another structure with a lower (local-minimum) energy. This way, a fully relaxed equilibrium geometry is obtained for each of the calculated structures.

The face centered cubic (fcc) Ge(111) surface has three types of sites that exhibit threefold rotational symmetry: (1) Sites above the top Ge atoms (green Ge atoms in Fig. 10), (2) sites above Ge atoms of the second layer (blue Ge atoms in Fig. 10), and (3) hollow sites (i.e., above Ge atoms of the fourth layer). Since we place the Ge atoms of our Ge(111) model initially at their bulk positions, the surface has a high density of broken bonds, i.e., one dangling bond per top Ge atom, which is energetically unfavorable. The density of these dangling bonds is reduced by introducing "foreign" Ge adatoms. When positioning an adatom above a hollow site or a second-layer Ge atom, it will bind to three (nearest-neighbor) Ge surface atoms and only one dangling bond (of the adatom itself) remains. The introduction of Ge adatoms thus reduces the total amount of dangling bonds and hence gives rise to an energetically more favorable surface. In the experiments, adatoms are observed above second-layer Ge atoms only. In order to find the energetically most favorable Co/Ge geometry, we use all three types of sites that are available within the $\sqrt{13}R14^\circ$ SUC (i.e., 13 sites for each type) as the initial coordinates of "foreign" Co and Ge atoms. For the Co atoms, the top Ge atom sites appear to be relevant only when considering bilayer Co structures that are formed at higher Co coverage and, as will be demonstrated in the following, these sites can be excluded here. For the Ge adatoms the sites above the second-layer Ge atom as well as the hollow sites need to be considered. Adsorption of Ge adatoms at these sites is found to yield a very similar energy gain,[79] and the possible interaction with Co atoms may imply that the hollow sites are more preferable for the Ge adatoms. Our calculations reveal that the Co atoms typically relax towards the hollow sites, regardless of their starting position. Co adsorption at these locations yields a lower total energy when compared to those geometries for which the Co atoms are found to stay above Ge atoms of the second Ge layer after relaxation. Furthermore, when a Co atom is placed at a hollow site, the top Ge atoms are found to relax upward to positions somewhat above the Co atoms (up to 1.4 Å). This finding is in line with our previous work, which demonstrated that Co atoms deposited on bare Ge(111)2×1 surfaces can penetrate down to the fourth Ge subsurface layer.[80,81]

If our candidate model system configurations would all have the same amount of atoms and only a different atomic geometry, the relaxed geometry that matches the $\sqrt{13}R14^\circ$ reconstruction could simply be determined by comparing the total energies of the different model system configurations and finding the energetically most favorable geometry. Here, however, it is not *a priori* known how many "foreign" atoms (i.e., Co atoms and Ge adatoms) contribute to the observed $\sqrt{13}R14^\circ$ reconstruction and need to be included in our model system. Therefore, the total energies of different model system configurations having a different amount of atoms can not be simply compared. For example, the minimum total energy of the Ge model system is that of the (2×1) reconstruction without any "foreign" atoms. The amount of possible configurations further increases when considering possible penetration of the Co atoms in subsurface Ge layers and the possible formation of bilayer Co structures. The atomic structure that matches the $\sqrt{13}R14^\circ$ reconstruction can therefore only be determined by direct comparison of DFT based simulations of STM topography images and experimental STM topography images. Comparison of filled-states and empty-states topography images reveals that only 1 atomic-structure model out of more than 40 candidates (with varying bonding geometry and stoichiometry) fully matches the experimental observations.

B. Structural model of Co/Ge(111)$\sqrt{13}R14°$ reconstruction

Figure 11 presents a ball-and-stick model of the atomic structure that is found to match to the experimentally observed Co/Ge(111)$\sqrt{13} \times \sqrt{13}\,R13.9°$ reconstruction. The structure contains one Ge adatom (red sphere) and six Co atoms (yellow spheres). The initial positions (prior to relaxation) of the "foreign" atoms are presented in Fig. 10. The six Co atoms are located vertically above hollow sites and have an equilateral triangular arrangement. The Ge adatom is initially located asymmetrically with respect to the Co triangle, i.e., vertically above a Ge atom of the second layer. In Fig. 11, we present a top and side view of the seven topmost layers after relaxation: six relaxed Ge layers and one layer of adsorbed Co and Ge atoms. For the lower-lying Ge layers, we maintain their initial (prior to relaxation) numbering, despite their strong reconstruction upon relaxation. The new top layer thus consists of one Ge adatom (red sphere) and the Ge atoms of the initial top layer (green spheres). A more detailed classification of the topmost atoms according to their height and electronic properties will be given below. The Ge atoms of the second layer (blue spheres) also considerably change their position during the relaxation, both laterally in the x, y plane as well as vertically in the z direction. The nearest neighbors of the Ge adatom,

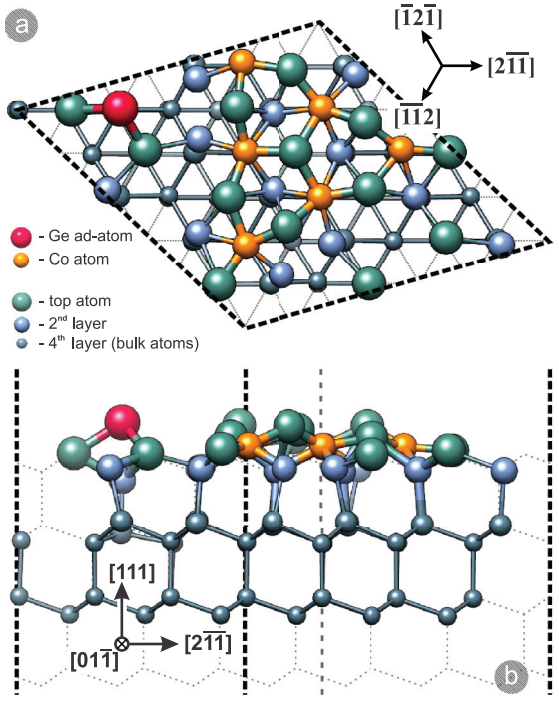

FIG. 11. (Color online) Ball-and-stick model of the *RIGHT*Co/Ge(111)$\sqrt{13}R14°$ reconstruction. (a) Top and (b) side views of the geometry presented in Fig. 10 after relaxation. The basis unit of the $\sqrt{13}R14°$ reconstruction consists of one Ge adatom (red sphere) and six Co atoms (yellow spheres). Green and blue colored spheres represent the Ge atoms of the first and second layers, respectively, similar to Fig. 10. The smaller gray-green spheres correspond to the bulk Ge atoms. The relaxed Co atoms are all located in-between the first and second Ge layers. The SUC is indicated by the dashed black rhombus in (a) and by vertical dashed black lines in (b), respectively. The initial positions of the bulk Ge atoms are indicated by the thin dotted mesh.

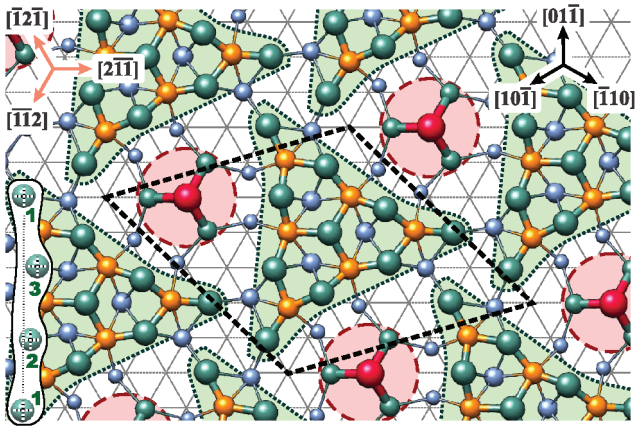

FIG. 12. (Color online) Top view of the upper two atomic layers of the Co/Ge(111)$\sqrt{13}R14°$ surface reconstruction based on the relaxed atomic structure presented in Fig. 11. The "building units" of the $\sqrt{13}R14°$ reconstruction are indicated by dashed red circles and green dotted triangles (see text for more details). The SUC of the $\sqrt{13}R14°$ reconstruction (indicated by the dashed black rhombus) is rotated over an angle $+13.9°$ with respect to the [$\bar{1}2\bar{1}$] direction, while the "building unit" indicated by the green dotted triangle is aligned to the crystallographic directions indicated in the upper left corner of the figure. The ideal fcc(111) surface mesh is indicated by gray thin dotted lines in the background. The colors of the different types of surface atoms are the same as the colors in Figs. 10 and 11.

i.e., three top Ge atoms, relax towards each other, while the Ge atoms of the second layer below the adatom move downwards. As a result, the Ge atoms of the third and fourth layers below the adatom [see Fig. 11(b)] move downwards as well. The Co atoms retain their triangular arrangement after relaxation and are all retrieved in-between the first and second Ge layers at about the same z position [see Fig. 11(b)]. The positions of the Ge bulk atoms below the fourth atomic layer are found to change only slightly after relaxation.

The relaxed model is visualized alternatively at larger scale in Fig. 12, where only the atoms from the two topmost Ge layers and the additional Co layer are included. This way, it can be seen that the Ge adatom is positioned symmetrically with respect to the surrounding Co triangles. Indeed, the Ge adatom is bonded to three top-layer Ge atoms [as is also the case for the $c(2 \times 8)$ reconstructed Ge surface].[79] These four Ge atoms can be considered as a "building unit" of the surface reconstruction and are indicated by a dashed red circle in Fig. 12. The six Co atoms and the surrounding 10 Ge atoms from the top and second Ge layers that interact with the Co atoms form another "building unit" of the surface reconstruction and are indicated by the green dotted triangle in Fig. 12. Figure 12 illustrates that the triangular building units are aligned with the crystallographic [$\bar{1}2\bar{1}$], [$2\bar{1}\bar{1}$], and [$\bar{1}\bar{1}2$] directions. The angle β is hence equal to zero for this triangular building unit. Note that the SUC of the $\sqrt{13}R14°$ reconstruction is tilted by an angle $\alpha = +13.9°$ with respect to the [$\bar{1}2\bar{1}$] direction, consistent with the experimentally observed $RIGHT\sqrt{13}$ orientation of the surface reconstruction discussed in Sec. III C.

The 10 Ge atoms of the triangular building unit [because of the analogy with the $c(2 \times 8)$ reconstruction again referred to as Ge rest atoms hereafter] relax significantly both laterally

and vertically. Their relaxation is not symmetrical due to the asymmetric position of the Ge adatom with respect to the triangular building unit. The Ge adatom induces "bending" of the side of the triangle formed by four Ge rest atoms adjacent to the Ge adatom. In the lower left part of Fig. 12, the center of the relaxed Ge rest atoms labeled (1)–(3) is highlighted by black-white dotted crosses. A straight dotted line is drawn in-between the two Ge rest atoms (1) located at the two corners of the triangular building unit. The largest relaxation occurs for the Ge rest atom that is located directly adjacent to the Ge adatom, i.e., Ge rest atom (3). Due to the translational periodicity of the two building units, the triangular unit is surrounded by Ge adatoms on three sides that all induce an identical "bending" of the sides of the triangular building unit. This is depicted by the green dotted deformed triangles in Fig. 12. The triangular building unit, alone and as well as in combination with the Ge adatom building unit, can hence be considered as a chiral structure.

The asymmetric position of the Ge adatom with respect to the triangular building block gives rise to the possibility to form either the $RIGHT\sqrt{13}$ or the $LEFT\sqrt{13}$ Co/Ge surface reconstruction. On the fcc Ge(111) surface, the Ge adatoms occupy two different, yet physically equivalent, positions, as illustrated in the central part of Fig. 13: The Ge adatom can be located both at the left-hand side (green dotted circle) and at the right-hand side (red dotted circle) of the triangular building unit (yellow dotted triangle), yielding a $RIGHT\sqrt{13}$ (green rhombus) and $LEFT\sqrt{13}$ (red rhombus) SUC. The $RIGHT\sqrt{13}$ and $LEFT\sqrt{13}$ SUCs are repeated twice in the right and left parts of Fig. 13, respectively, to illustrate the symmetry of the Ge adatom positions in-between the triangular building units for both SUCs. Calculations for the $LEFT\sqrt{13}$ SUC (using CG geometry optimization and DFT based simulations of STM topography images) reveal that the geometry and electronic properties of the $LEFT\sqrt{13}$ surface reconstruction is identical to that of the $RIGHT\sqrt{13}$ surface reconstruction. The bending of the three sides of the triangular building unit of both geometries is the same, yielding the chiral structures that exhibit mirror symmetry with respect to each other, as observed in the experiments discussed in Sec. III C. It is still under question if the triangular Co structures grow first and the Ge adatoms arrive afterwards, or that the Ge adatoms grow first and that their positions determine the positions for growth of the triangular Co building blocks.

From Fig. 12 it becomes clear that the Co/Ge(111)$\sqrt{13}R14^\circ$ surface reconstruction can be "constructed" using the larger building unit formed by the smaller Ge adatom and triangular Co/Ge building units (see Fig. 14). As already mentioned above, the Ge rest atoms considerably change their position in the vertical direction upon relaxation, resulting in a different height for each Ge rest atom. We can distinguish four types of Ge rest atoms in the triangular Co/Ge building unit: (1) three Ge atoms at corner positions [$Ge_{(1)}$], (2) three Ge atoms at side positions [$Ge_{(2)}$], (3) three Ge atoms at side positions close to the Ge adatom [$Ge_{(3)}$], and (4) one Ge atom at the center of the

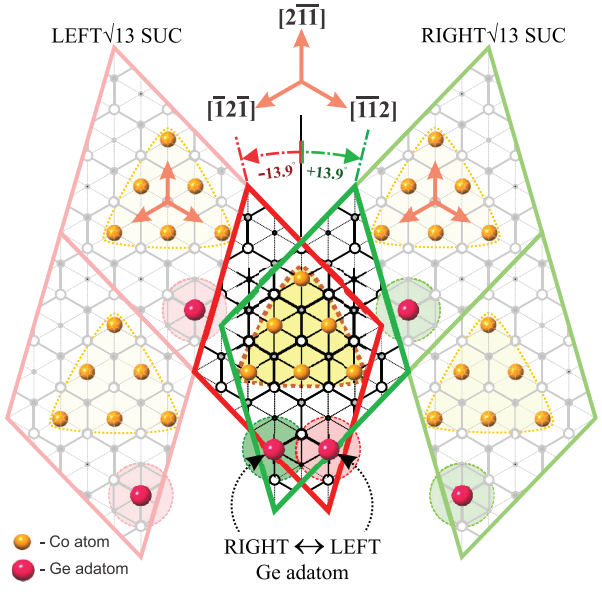

FIG. 13. (Color online) Sketch of the two possible positions of Ge adatoms on the Ge(111)(1×1) surface with respect to the triangular building units formed by Co atoms. The Ge adatom (red sphere) building units are indicated by green and red dotted circles enclosing a red colored Ge adatom, while the six Co atoms (yellow spheres) of the triangular building units are indicated by the yellow dotted triangle. The two positions of the Ge adatom, labeled $RIGHT$ and $LEFT$, give rise to two different SUCs, i.e., a $RIGHT\sqrt{13}$ SUC (green rhombus) and a $LEFT\sqrt{13}$ SUC (red rhombus). The $RIGHT\sqrt{13}$ and $LEFT\sqrt{13}$ SUC surfaces are repeated twice in the right and left parts of the figure, respectively.

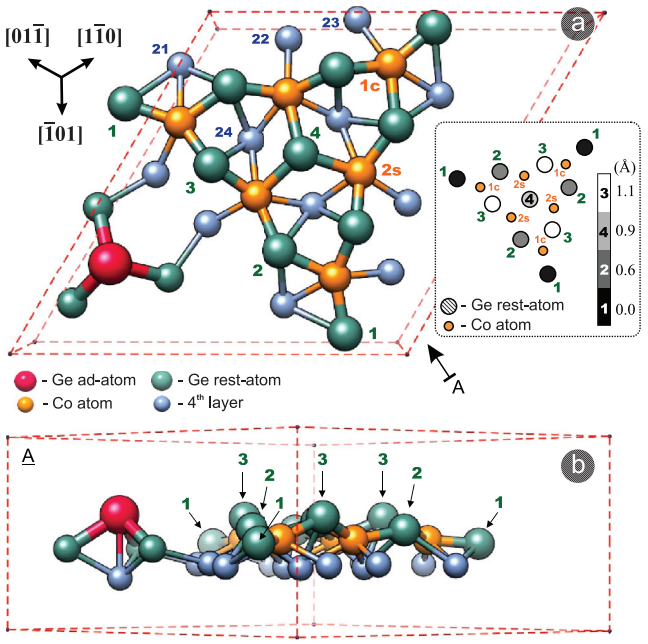

FIG. 14. (Color online) (a) Top and (b) side views of a ball-and-stick model of the Ge adatom and triangular Co/Ge building unit of the Co/Ge(111)$\sqrt{13}R14^\circ$ surface reconstruction. In (b) the atomic structure is viewed along the direction indicated by the arrow labeled A in (a). The inset in (a) indicates the relative height of the relaxed Ge rest atoms within the triangular building unit. The numbers on the gray height scale bar indicate the different heights of the Ge rest atoms in (a) and (b). The SUC is indicated in (a) and (b) by a 3D red dashed rhombus (its height in the [111] direction is chosen arbitrarily).

TABLE I. Calculated distances between the two types of Co atoms and the neighboring Ge rest atoms (labeled in Fig. 14).

Atom pair	Co–Ge Distance
$Co_{(1c)}$–$Ge_{(1)}$	2.204 Å
$Co_{(1c)}$–$Ge_{(2)}$	2.365 Å
$Co_{(1c)}$–$Ge_{(3)}$	2.262 Å
$Co_{(1c)}$–$Ge_{(21)}$	2.475 Å
$Co_{(1c)}$–$Ge_{(22)}$	2.430 Å
$Co_{(2s)}$–$Ge_{(2)}$	2.294 Å
$Co_{(2s)}$–$Ge_{(3)}$	2.261 Å
$Co_{(2s)}$–$Ge_{(4)}$	2.471 Å
$Co_{(2s)}$–$Ge_{(22)}$	2.390 Å
$Co_{(2s)}$–$Ge_{(23)}$	2.473 Å
$Co_{(2s)}$–$Ge_{(24)}$	2.504 Å

triangular building unit [$Ge_{(4)}$]. The three atoms of types (1)–(3) exhibit identical properties, i.e., they are at the same height and have the same bond distances, atom population, and Mulliken overlap population with deviations for each of these parameters remaining below 0.05%. The inset in Fig. 14(a) gives the relative height of the relaxed $Ge_{(1)}$–$Ge_{(4)}$ rest atoms. The $Ge_{(1)}$ atoms have the lowest position within the triangular building unit, while the $Ge_{(2)}$, $Ge_{(4)}$, and $Ge_{(3)}$ atoms are located 0.6, 0.9, and 1.1 Å above the $Ge_{(1)}$ atoms, respectively. The Co atoms all have the same height, i.e., below the $Ge_{(2)}$ atoms and 0.1 Å above the $Ge_{(1)}$ atoms. Based on their identical properties, the six Co atoms can be divided into two subgroups: (1) three Co atoms at corner positions [$Co_{(1c)}$] and (2) three Co atoms at side positions [$Co_{(2s)}$] [see Fig. 12(a)]. Similarly, the 12 Ge atoms of the second layer can be divided into 4 subgroups: (1) three Ge atoms bonded to $Co_{(1c)}$, $Ge_{(1)}$, and $Ge_{(2)}$ atoms [$Ge_{(21)}$], (2) three Ge atoms bonded to $Co_{(2s)}$ atoms [$Ge_{(22)}$], (3) three Ge atoms bonded to $Co_{(1c)}$ atoms [$Ge_{(23)}$], and (4) three Ge atoms located inside the Co triangle [$Ge_{(24)}$]. The distances between the different Co–Ge atoms of the relaxed $\sqrt{13}R14^\circ$ model are listed in Table I. The covalent bond length of the Ge adatom is found to be 2.633 Å, which is slightly larger (8%) than for typical bulk Ge–Ge bonds (2.439 Å) and consistent with previous studies.[79,82]

C. DFT based modeling of STM topography images and electronic structure of the Co/Ge $\sqrt{13}R14^\circ$ surface reconstruction

To confirm our Co/Ge $\sqrt{13}R14^\circ$ model, we compare the experimental constant current STM topography images to simulated STM topography images. The simulated STM images are obtained using the Tersoff-Hamann approximation[83,84] at a distance of several angstroms above the position of the topmost surface atoms. The dependence of the tunneling current I on the tunneling voltage V between the STM tip and the surface is

$$I = \frac{2\pi e}{\hbar} \sum_{\mu,v} f(E_\mu)[1 - f(E_v + eV)] \mid M_{\mu v} \mid^2 \delta(E_\mu - E_v), \quad (1)$$

where $f(E)$ is the Fermi-Dirac distribution function, $M_{\mu v}$ is the tunneling matrix element between electronic states ψ_μ of the tip and electronic states ψ_v of the surface, and E_μ (E_v) are the energies of the states ψ_μ (ψ_v) in the absence of tunneling. When we assume localized wave functions ψ_μ for the tip, $M_{\mu v}$ is proportional to the amplitude of ψ_v at position $\vec{r}_0$ of the probing tip at low temperatures. For small tunneling voltages V, Eq. (1) reduces to

$$I \propto \sum_v \mid \psi_v(\vec{r}_0) \mid^2 \delta(E_\mu - E_F). \quad (2)$$

Following Eq. (2), the tunneling current I is proportional to the surface LDOS that is probed at position $\vec{r}_0$ of the tip, integrated over an energy range from E_F to $E_F + eV$. For a constant tunneling current I the STM tip essentially follows a contour of constant surface LDOS. However, because the surface wave functions decay exponentially into the vacuum region, numerical evaluation of $\psi_v(\vec{r}_0)$ (within the DFT based approach these are the Kohn-Sham wave functions of the surface) for tip-surface distances of the order of several angstroms poses a significant problem for the DFT based calculations. For this reason, STM simulations are often restricted to (the vicinity of) the surface, which may yield incorrect results. In order to tackle this problem, we use the 2D Fourier transform of the wave functions $\psi_v(\vec{r})$ in combination with spatial extrapolation techniques[85] to evaluate the surface wave functions $\psi_v(x,y,z_0)$ in the vacuum region, up to $z_0 = 10$ Å above the surface. We rely on an experimental $z(V_t)$ spectrum measured on the $\sqrt{13}R14^\circ$ surface to take into account the dependence of the height z on the tunneling voltage V_t in our calculations. This $z(V_t)$ dependence, to which an initial tip-sample distance of 3 Å is added, is used to determine the height above the surface at which simulated STM images are calculated. For low voltages, i.e., for energies close to E_F, $z(V_t) \simeq 3.5$ Å, while for high voltages above 1 V, $z(V_t) \gtrsim 6.4$ Å.

This way, we calculate STM topography images for all possible Co/Ge conformations for the filled-states and empty-states regimes between −3.0 and +3.0 eV. Agreement between theory and experiment is achieved for the entire energy range only for the relaxed model presented in Fig. 11. In Fig. 15, we present a series of experimental (outer columns, grayscale images) and calculated (inner columns, color scale rhombus) STM constant current topography images for the filled-states (two right columns) and empty-states (two left columns) regimes. Calculated STM topography images are obtained for a 3×3 SUC (indicated by the dashed white-blue rhombus) for the $RIGHT\sqrt{13}$ geometry displayed in Fig. 11. Experimental STM topography images in Fig. 15 are all recorded at the same location.

Initially, the $\sqrt{13}R14^\circ$ SUC rhombus was chosen based on high-bias empty-states STM images (see Sec. III D) and the corners of the SUC rhombus were positioned on the bright atomic features without any further knowledge of the origin of these bright features. Following our proposed model, these features stem from the Ge adatoms. We therefore redefine (using a parallel translation operation) the $\sqrt{13}R14^\circ$ SUC rhombus in the calculated images with respect to the experimental STM images (white dotted rhombus in Fig. 15). Furthermore, the $\sqrt{13}R14^\circ$ building unit discussed in the

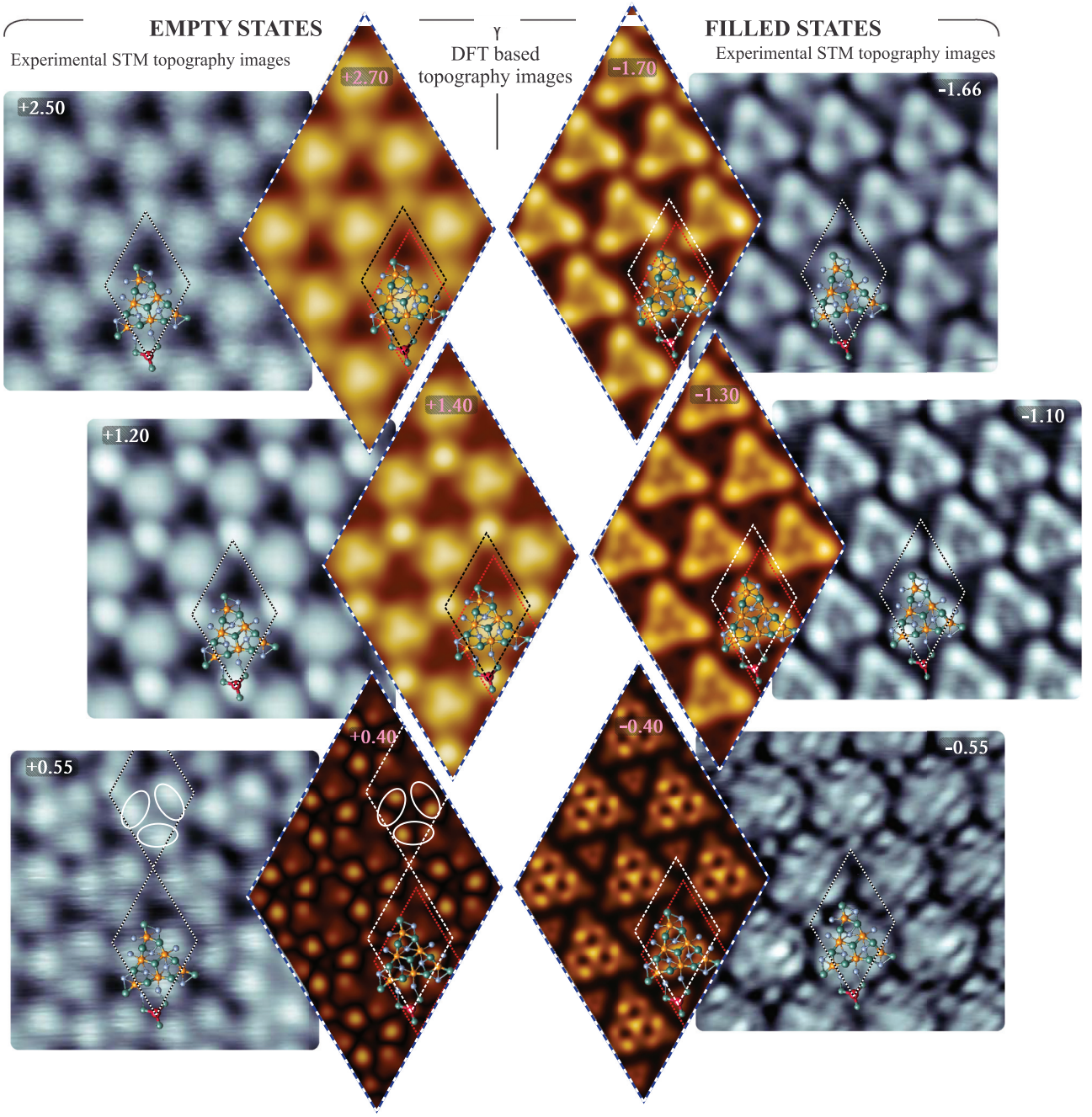

FIG. 15. (Color online) Experimental empty-states and filled-states STM topography images (outer columns, grayscale images) and the corresponding simulated STM topography images (inner columns, color scale rhombus) of the Co/Ge(111)$\sqrt{13}R14^\circ$ surface reconstruction. The tunneling voltage V_t is indicated in each of the images. Two $\sqrt{13}R14^\circ$ SUCs are indicated in the simulated images: A red dotted rhombus SUC used for the calculations and a white dotted rhombus SUC inferred from the experimental images (see Sec. III D). The $\sqrt{13}R14^\circ$ "building unit" (see Fig. 14) is superimposed on each image at exactly the same location.

previous section is superimposed on each image at exactly the same location.

The calculated STM images nicely reproduce all of the important features of the experimental STM images in Fig. 15. In the filled-states regime, perfect agreement between experiment and theory is achieved for the entire tunneling voltage range. For the empty-states regime, perfect agreement is found as well, except for the lowest tunneling voltages, where small differences can be observed. These small discrepancies can be attributed to the approximations made in the DFT calculations (see discussion below).

In the filled-states regime, at tunneling voltages below -0.9 V, the calculated topography becomes dominated by an equilateral triangular feature that exhibits bright protrusions above the $Co_{(1c)}$ atoms (see Fig. 15). Upon more careful analysis, we find that this electronic feature originates from a complex contribution of hybridized orbitals of the $Co_{(1c)}$ and $Ge_{(3)}$ atoms to the integrated LDOS probed above the surface.

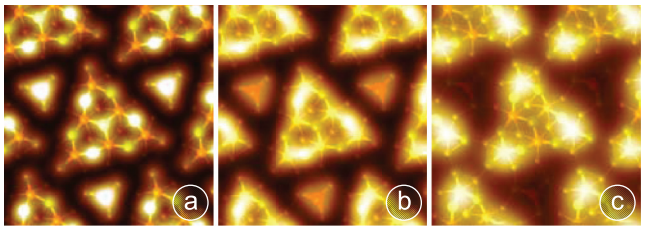

FIG. 16. (Color online) Height dependence of high-bias filled-states calculated DFT based STM topography images. The height above the surface at which the STM images are calculated is (a) 3.5 Å, (b) 4.0 Å, and (c) 6.2 Å. All images are calculated for the same tunneling voltage $V_t = -1.6$ V. The first two surface layers of the Co/Ge $\sqrt{13}R14^\circ$ model are added below the topography images that are made semitransparent.

The dependence of these local LDOS maxima on the height above the surface is illustrated in Fig. 16. At lower heights close to the surface, the LDOS is dominated by the topmost atoms, i.e., the Ge adatom and the $Ge_{(3)}$ atoms [see Fig. 16(a)]. With increasing distance from the surface, their contribution to the integrated LDOS rapidly decays [see Fig. 16(b)], in contrast to the contribution from the $Co_{(1c)}$ atoms that in turn start to dominate the LDOS at larger distances from the surface [see Figs. 16(b) and 16(c)]. At heights above 4.5 Å only states related to the $Co_{(2c)}$ atoms are observed both theoretically and experimentally. At lower voltages in the filled-states regime the fine structure of the upper atoms within the triangular building unit appears, with the Ge atoms being more pronounced than the Co atoms (Fig. 15). This fine structure can not be resolved in the experimental STM image due to STM tip convolution effects that hamper visualization of such small corrugations. Nevertheless, the main features in the calculated and experimental images are in very good agreement and the Ge adatom can be clearly traced in both images.

In order to shed more light on the contribution of Co and Ge rest atoms to the electronic properties, we also perform density of states (DOS) calculations. Plots of the projected DOS for different atom sites are presented in Figs. 17(b) and 17(c), while Fig. 17(a) presents the total DOS and the surface DOS (topmost two Ge atomic layers and Co layer). In addition, Fig. 18 provides a direct comparison of the experimental $(dI/dV)/(I/V)$ spectra of the $\sqrt{13}R14^\circ$ reconstructed nanoisland and the theoretical surface DOS of the Co/Ge $\sqrt{13}R14^\circ$ slab. The experimental $(dI/dV)/(I/V)$ spectrum is obtained by area averaging CITS data of the locations labeled (1)–(3) in Fig. 8 for different Co/Ge $\sqrt{13}R14^\circ$ nanoislands. From comparison of Figs. 17(b) and 17(c), it is clear that the valence band (VB) is dominated by the *d* states stemming from the Co atoms, while the *sp* states of the Ge surface atoms exist in the conduction band. The contribution of the Co atoms to the DOS [see black dashed curve in Fig. 17(b)] exhibits maxima around −0.8 eV that lie well outside the bulk Ge band gap [Fig. 17(a)] and below the top of the VB. These maxima are split by 0.3 eV due to the presence of two types of Co atoms, i.e., a $Co_{(1c)}$ and a $Co_{(2s)}$ atom. The absolute values of the peaks are the same for the $Co_{(1c)}$ and $Co_{(2s)}$ atom [see red and blue dashed curves in Fig. 17(b)]. The integrated LDOS above the surface is, however, dominated by the $Co_{(1c)}$ atoms. The $Co_{(2s)}$

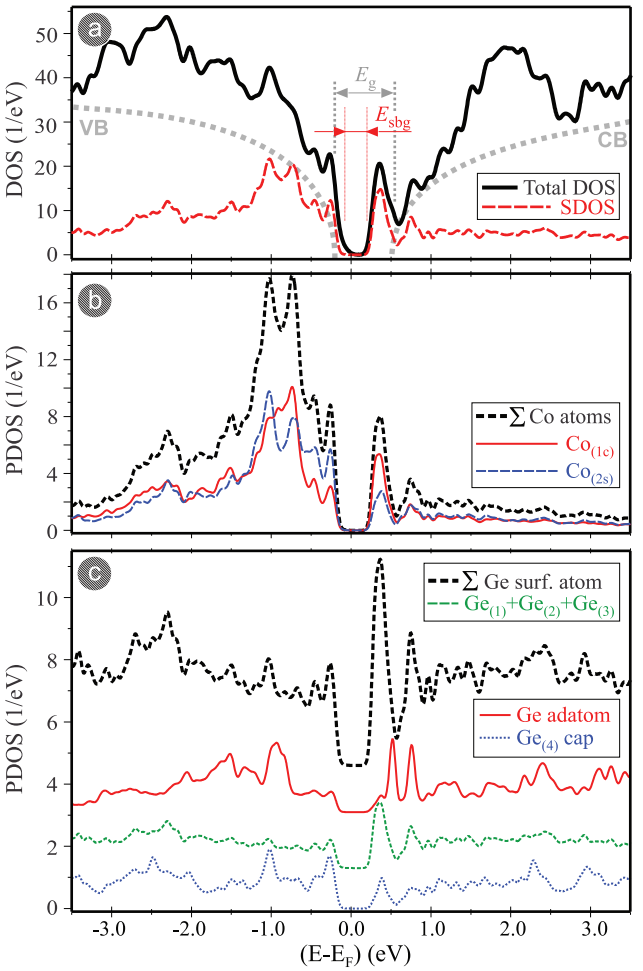

FIG. 17. (Color online) (a) Total DOS (black curve) and surface DOS (red dashed curve) for the Co/Ge $\sqrt{13}R14^\circ$ slab. (b) Site projected DOS of a $Co_{(1c)}$ atom (red solid curve), a $Co_{(2s)}$ atom (blue dashed curve), and the sum of both DOSs (black dashed curve). (c) Site projected DOS of all Ge atoms from the top layer (black dashed curve), partial DOS of a Ge adatom (red solid curve), a $Ge_{(4)}$ atom (blue dotted line), and the sum of the $Ge_{(1)}$, $Ge_{(2)}$, and $Ge_{(3)}$ rest atoms (green dashed line). Curves are shifted vertically for clarity.

atoms have a smaller contribution to the LDOS, resulting in less pronounced spots in the triangular building unit. It can hence be concluded from Figs. 17(a) to 17(c) that the surface DOS of the VB stems mainly from the Co atoms, in agreement with the experimental STS measurements (see Fig. 18). The surface state S_{2F} can be directly attributed to $Co_{(1c)}$ and $Co_{(2s)}$ surface atoms, while the surface state S_{1F} is associated with a different contribution of the Co and Ge atoms.

In the empty-states regime at tunneling voltages above 0.7 V, the calculated topography is dominated by the Ge adatom, which exhibits maximum contrast around 1.3 V (see Fig. 15), and by the $Ge_{(3)}$, $Ge_{(2)}$, and $Ge_{(4)}$ rest atoms, which appear as the "central" bright protrusion. The latter feature becomes more pronounced with increasing tunneling voltage and above 1.8 V it is brighter than the Ge adatom, whose brightness decreases with increasing tunneling voltage (see Fig. 15). At low tunneling voltages, the calculated and experimental images exhibit some discrepancies. In particular,

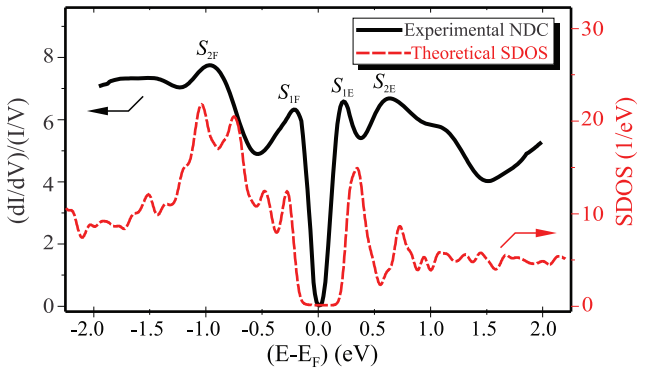

FIG. 18. (Color online) Comparison of a typical experimental $(dI/dV)/(I/V)$ spectrum of a $\sqrt{13}R14°$ reconstructed nanoisland (black solid curve) and the theoretical surface DOS of the Co/Ge $\sqrt{13}R14°$ slab (red dashed curve).

a fine structure related to the $Ge_{(3)}$ and $Ge_{(2)}$ rest atoms is found in the calculated images, while the experimental images reveal three broadened spots per SUC at the locations of the $Co_{(2s)}$ atoms. The DOS calculations indicate that the Ge and Co atoms exhibit peaks in the bulk band gap around 0.3 eV, which can be considered as surface states [see Figs. 17(b) and 17(c) and the surface state S_{1E} in Fig. 18]. The interplay between these states hence determines the integrated LDOS above the surface in the empty-states regime at low tunneling voltages. According to our DFT based calculations, the $Ge_{(3)}$ and $Ge_{(2)}$ atoms have a larger contribution to the integrated LDOS, which is in disagreement with the experimental observations. This disagreement can be explained as follows. First, the three experimentally observed spots may indeed be related to $Ge_{(3)}$ and $Ge_{(2)}$ rest atoms. These atoms can form a hybridized state that gives rise to the large broadened spots in the STM images. This is indicated in the extra SUC rhombus drawn in the experimental and calculated images in Fig. 15. The three white ellipses drawn in this SUC indicate the coupling between the $Ge_{(3)}$ and $Ge_{(2)}$ atoms that can give rise to three large broadened spots per SUC. Second, we note that the calculations do not take into account effects such as tip-induced band bending, resonant tunneling, and nonequilibrium effects.[60,86] These effects may result in a shift of the energy levels of the surface states, which is evident from comparison of the experimental $(dI/dV)/(I/V)$ spectrum to the theoretical surface DOS spectrum in Fig. 18. The here encountered discrepancy between theory and experiment can be related to the well-known fact that DFT is not able to reliably reproduce the size of the band gap of semiconductor materials. Because doping of the Ge substrate is not included in our DFT based calculations, our DOS calculations predict the presence of a pseudogap with a negligible DOS around E_F that separates the bonding from the antibonding states [see Fig. 17(a)]. However, our STS measurements indicate a metallic-type conductivity for the Co/Ge $\sqrt{13}R14°$ nanoislands (see Fig. 18 and also the discussion in Sec. III E). We therefore believe that inclusion of the tunneling and doping effects in a spin-dependent calculation will resolve the here observed discrepancy between theory and experiment at low tunneling voltages.

The amount of possible chemical bonds of the Co and Ge atoms can be estimated from an analysis of their bond lengths (see Table I). For a single bond between a Co and a Ge atom, the bond length can be estimated as the sum of the Co and Ge covalent radii, which is $r_c = 2.38$ Å. Analysis of the calculated $Co_{(1c)}$–$Ge_{(x)}$ and $Co_{(2s)}$–$Ge_{(x)}$ distances reveals that all Co–Ge pairs form chemical bonds, since all distances differ from r_c by only -7.4% to $+3.9\%$, only the $Co_{(2s)}$–$Ge_{(24)}$ distance is somewhat larger (5.2%). An underestimation of the bond lengths by a few percent is typical for DFT based calculations. The chemical bonding mechanism between the Co and Ge atoms involved in the DFT electronic-structure calculations can be investigated in more detail by evaluating the crystal orbital overlap population/Hamiltonian population (COOP/COHP).[87,88] We use an alternative COOP/COHP based approach that allows us to calculate the relevant physical quantities independent of the choice of the zero of the potential by relying on the so-called covalent bond energy (ECOV).[89] COOP and ECOV calculations are known to yield similar results, while the COOP method generally overestimates the magnitude of the antibonding states when defined for a plane-wave basis set.[90] Figure 19 presents the partial E_{COV} for $Co_{(1c)}$–$Ge_{(x)}$, $Co_{(2s)}$–$Ge_{(x)}$, and $Ge_{(x)}$–$Ge_{(x)}$ interactions. Negative, positive, and zero values of E_{COV} correspond to bonding, antibonding, and nonbonding interactions, respectively. Above the Fermi level, the E_{COV} spectra reflect a pronounced bonding

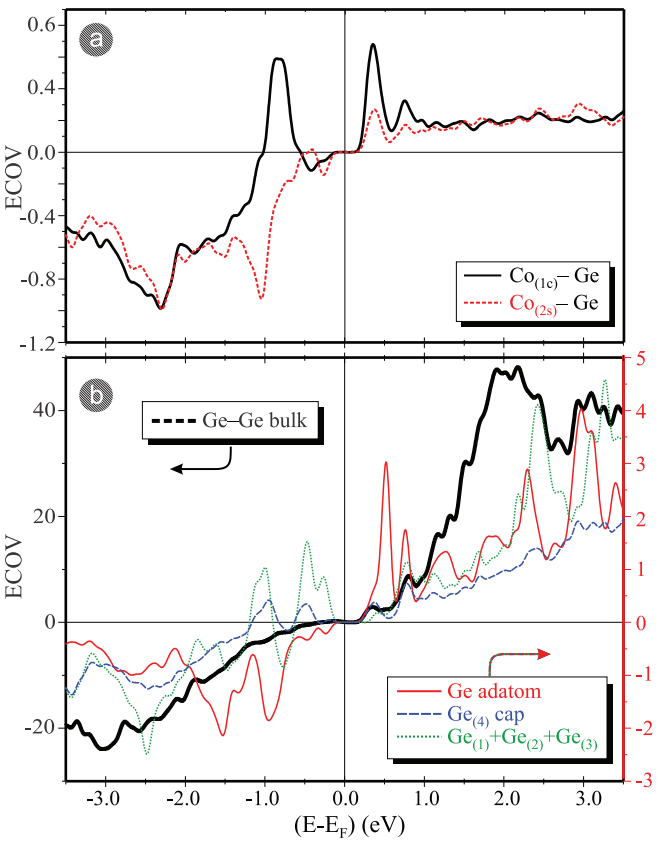

FIG. 19. (Color online) Chemical bonding in terms of the covalent bond energy E_{COV}. (a) $Co_{(1c)}$–Ge and $Co_{(2s)}$–Ge interactions. (b) Ge–Ge bulk (black curve) and Ge (surface atom)–Ge/Co interactions (colored curves).

TABLE II. Mulliken overlap population and electron population for the Co/Ge $\sqrt{13}R14^\circ$ reconstruction. Co and Ge atoms are numbered according to Fig. 14 and Table I.

Atom/atom	$Co_{(1c)}$	$Co_{(2s)}$	Electron pop.
Ge(1)	0.235		3.939
Ge(2)	0.139	0.217	4.210
Ge(3)	0.193	0.222	4.123
Ge(4)		0.152	4.351
Ge(21)	0.124		4.181
Ge(22)		0.206	4.139
Ge(23)	0.167		4.163
Ge(24)		0.161	4.273
Ge(24)	0.077	0.146	4.273
Electron pop.	8.552	8.440	

character of the Co–Ge and the Ge–Ge interactions (see Fig. 19). Near −0.8 eV the E_{COV} spectrum indicates an antibonding interaction between the $Co_{(1c)}$ and the neighboring Ge rest atoms. The latter also exhibit antibonding peaks around −0.5 and −1.05 eV. This may be linked to the instability of the Co/Ge system in nonmagnetic configurations and to the known thermal instability of the Co/Ge complex.

Using Mulliken population analysis,[91] we can investigate in more detail the character of the bonds involved in the Co/Ge $\sqrt{13}R14^\circ$ reconstruction. The positive and negative overlap population values indicate bonding and antibonding states, respectively. The partial Mulliken electron orbital overlap populations of the Co atoms and the electron populations are listed in Table II. The calculations reveal that significant charge redistribution occurs between the Co atoms and the Ge surface atoms, i.e., $0.45|e|$ and $0.56|e|$ are transferred to the neighboring Ge atoms from $Co_{(1c)}$ and $Co_{(2s)}$, respectively (see Table II). Such densities of transferred electrons indicate a weak bonding with ionic or metallic-covalent character. The $Co_{(1c)}$ and $Co_{(2s)}$ atoms exhibit five and six discernible bonds with Mulliken overlap populations, respectively. The overlap of the atomic orbitals is 35% to 58% of that of the Ge–Ge bulk covalent bond (approximately 0.4). The Ge adatom has a neutral charge and three covalent bonds with an overlap of 40% to 50% of that of the Ge–Ge bulk covalent bond. There also exists a weak interaction between the $Co_{(1c)}$ and $Ge_{(24)}$ atom (see Table II). Because of the very low overlap population (17% of Ge–Ge bulk covalent bond overlap), this interaction should not be considered as a sixth bond. It can be seen in Table II that all values of the bond overlap population are positive, yet relatively small, which indicates that there exist ionic or metallic-covalent interactions between the populations. Our findings based on the bond length and the Mulliken overlap population analysis are in good agreement with the calculated electron charge density distribution $\rho(x,y,z)$ (data not shown), where zones of high electron localization (the signature of chemical bonds) between the Co and Ge atoms are found to appear gradually at isosurface values below 0.06 e/Å^3. The $Co_{(1c)}$ and $Ge_{(24)}$ pair do not exhibit any remarkable electron localization. We therefore conclude that the $Co_{(1c)}$ and $Co_{(2s)}$ atoms form bonds with five and six neighboring Ge atoms, respectively. We note that our experimental conditions are in the temperature range where solid-state germanide phases such as CoGe,[21] Co_5Ge_7,[92] and $CoGe_2$ (Ref. 93) germanides are known to be formed. Here, however, we do not intend to provide a similar precise indication of the chemical formula of the Co/Ge $\sqrt{13}R14^\circ$ structure because the atomic geometry in our model is a planar system rather than an equilibrium bulk phase such as cubic CoGe, tetragonal Co_5Ge_7, or orthorhombic $CoGe_2$. Interpretation of our planar Co/Ge structure in terms of germanide phases is therefore left as an open question because for germanide phases the transition from a surface (planar) to a bulk (3D) structure is not well defined. Further analysis of the Co/Ge $\sqrt{13}R14^\circ$ atomic structure model in order to identify the proper analogy with the known germanide bulk phases will be the subject of our future research.

V. SUMMARY

Co/Ge(111)$\sqrt{13}R14^\circ$ reconstructed nanoislands are obtained by deposition of Co atoms on Ge(111)$c(2\times 8)$ surfaces and subsequent annealing. Relying on combined STM/STS measurements and DFT based calculations, the atomic structure of the Co/Ge(111)$\sqrt{13}R14^\circ$ surface reconstruction is determined. Both our experiments and our calculations demonstrated that the $\sqrt{13}R14^\circ$ reconstruction results from the mixing of Co and Ge without the need to involve a third element such as Ag.[45–47]

Voltage-dependent STM imaging reveals the coexistence of two inequivalent structural phases of the Co/Ge $\sqrt{13}R14^\circ$ surface reconstruction. The $RIGHT\sqrt{13}$ and $LEFT\sqrt{13}$ $\sqrt{13}R14^\circ$ reconstructed phases are found to be chiral structures, having a SUC that is rotated over an angle of $+13.9^\circ$ and -13.9° with respect to the $[2\bar{1}1]$ direction, respectively.

STS spectra of the $\sqrt{13}R14^\circ$ reconstructed Co/Ge(111) nanoislands reveal semimetallic behavior and a very small band gap that locally varies within the SUC between 10 and 250 meV. This is consistent with previously reported metallic properties of other germanide materials and offers potential for use as an Ohmic contact material. Spectra of the Ge surface surrounding the Co/Ge nanoislands reveal an electronic structure similar to that of bare Ge(111)$c(2\times 8)$ surfaces and are used as a reference. Spectra of the $\sqrt{13}R14^\circ$ reconstructed surface further reveal several additional states, including two surface states at ±0.2 V with respect to E_F, i.e., within the projected Ge bulk band gap. LDOS maps of $RIGHT\sqrt{13}$ and $LEFT\sqrt{13}$ reconstructed Co/Ge nanoislands recorded in a wide energy range show that the $RIGHT\sqrt{13}$ and $LEFT\sqrt{13}$ phases exhibit identical local electronic properties.

Based on these experimental findings, a model for the atomic structure of the $\sqrt{13}R14^\circ$ reconstructed Co/Ge(111) surface is obtained. DFT based simulations of the STM images for this model are in perfect agreement with the experimental STM images for the entire investigated range of tunneling voltages. In our model, each $\sqrt{13}R14^\circ$ SUC contains one Ge adatom located above a Ge atom of the second layer and six Co atoms located at *hollow sites* below the Ge surface layer in the form of an equilateral triangle. Ten Ge rest atoms relax upward due to the relaxation of the Co atoms to a position well below the surface. We find that the Ge adatom can occupy two different, yet physically equivalent, sites, located asymmetrically with respect to the Co triangle, which gives

rise to the $RIGHT\sqrt{13}$ and $LEFT\sqrt{13}$ chiral phases of the Co/Ge nanoislands.

The six Co atoms of the SUC can be divided into two subgroups: Atoms at corner positions ($Co_{(1c)}$) and at side positions ($Co_{(2s)}$) of the equilateral triangle. Filled-states STM images are dominated by $Co_{(1c)}$ derived states and to some extent also by $Co_{(2s)}$ derived states. The $Co_{(1c)}$ related brighter corners in the STM images are aligned along the $[2\bar{1}\bar{1}]$, $[\bar{1}\bar{1}2]$, and $[\bar{1}2\bar{1}]$ directions. Empty-states STM images are dominated by Ge adatom derived states and by the group of Ge rest atoms. In addition, we find that the interplay between the $Co_{(2s)}$ and Ge rest atoms determines the integrated LDOS above the surface at low tunneling voltages in the empty-states regime.

Finally, analysis of the covalent bond energy, Mulliken overlap populations, and charge density confirms the stability of the Co/Ge $\sqrt{13}R14^\circ$ structure and moreover reveals significant charge transfer between the Co atoms and Ge rest atoms. We conclude that the bonds involved in the Co/Ge $\sqrt{13}R14^\circ$ structure are dominated by nearest-neighbor interactions that have an ionic or metallic-covalent character. DFT based calculations of the Co–Ge bond strength further reveal that the $Co_{(1c)}$ and $Co_{(2s)}$ atoms form bonds with five and six neighboring Ge atoms, respectively.

ACKNOWLEDGMENTS

The research in Moscow has been supported by the Russian Foundation for Basic Research (RFBR) grants and by the computing facilities of the M. V. Lomonosov Moscow State University (MSU) Research Computing Center. The research in Leuven has been supported by the Research Foundation–Flanders (FWO, Belgium) as well as by the Flemish Concerted Action (GOA) research program.

*mda@spmlab.ru
†Koen.Schouteden@fys.kuleuven.be

[1] D. L. Harame, S. J. Koester, G. Freeman, P. Cottrel, K. Rim, G. Dehlinger, D. Ahlgren, J. S. Dunn, D. Greenberg, A. Joseph, F. Anderson, J. S. Rieh, S. A. S. T. Onge, D. Coolbaugh, V. Ramachandran, J. D. Cressler, and S. Subbanna, Appl. Surf. Sci. **224**, 9 (2004).
[2] R. Keyes, Rep. Prog. Phys. **68**, 2701 (2005).
[3] C. O. Chui, K. Gopalakrishnan, P. B. Griffin, J. D. Plummer, and K. C. Saraswat, Appl. Phys. Lett. **83**, 3275 (2003).
[4] H. Bracht, S. Schneider, J. N. Klug, C. Y. Liao, J. L. Hansen, E. E. Haller, A. N. Larsen, D. Bougeard, M. Posselt, and C. Wündisch, Phys. Rev. Lett. **103**, 255501 (2009).
[5] C. Claeys and E. Simoen, *Germanium-Based Technologies-From Materials to Devices* (Elsevier, Amsterdam, 2007).
[6] S. M. Sze and J. C. Irvin, Solid-State Electron. **11**, 599 (1968).
[7] T. Dietl, H. Ohno, F. Matsukura, J. Cibert, and D. Ferrand, Science **287**, 1019 (2000).
[8] S. A. Wolf, D. D. Awschalom, R. A. Buhrman, J. M. Daughton, S. von Molnár, M. L. Roukes, A. Y. Chtchelkanova, and D. M. Treger, Science **294**, 1488 (2001).
[9] G. A. Prinz, Science **250**, 1092 (1990).
[10] S. Cho, S. Choi, S. C. Hong, Y. Kim, J. B. Ketterson, B.-J. Kim, Y. C. Kim, and J.-H. Jung, Phys. Rev. B **66**, 033303 (2002).
[11] G. A. Prinz, Phys. Today **48**(4), 58 (1995).
[12] I. Žutić, J. Fabian, and S. Das Sarma, Rev. Mod. Phys. **76**, 323 (2004).
[13] P. Ryan, R. P. Winarski, D. J. Keavney, J. W. Freeland, R. A. Rosenberg, S. Park, and C. M. Falco, Phys. Rev. B **69**, 054416 (2004).
[14] J.-M. Tang, J. Levy, and M. E. Flatté, Phys. Rev. Lett. **97**, 106803 (2006).
[15] R. Hanson and D. D. Awschalom, Nature (London) **453**, 1043 (2008).
[16] R. Jaafar, D. Berling, D. Sébilleau, and G. Garreau, Phys. Rev. B **81**, 155423 (2010).
[17] K. Hamaya, T. Murakami, S. Yamada, K. Mibu, and M. Miyao, Phys. Rev. B **83**, 144411 (2011).
[18] T. Sadoh, H. Kamizuru, A. Kenjo, and M. Miyao, Appl. Phys. Lett. **89**, 192114 (2006).
[19] S. P. Ashburn, M. C. Öztürk, G. Harris, and D. M. Maher, J. Appl. Phys. **74**, 4455 (1993).
[20] S. Gaudet, C. Detavernier, C. Lavoie, and P. Desjardins, J. Appl. Phys. **100**, 034306 (2006).
[21] K. Opsomer, D. Deduytsche, C. Detavernier, R. L. V. Meirhaeghe, A. Lauwers, K. Maex, and C. Lavoie, Appl. Phys. Lett. **90**, 031906 (2007).
[22] J. E. Rowe, S. B. Christman, and G. Margaritondo, Phys. Rev. Lett. **35**, 1471 (1975).
[23] Y. Chang, Y. Hwu, J. Hansen, F. Zanini, and G. Margaritondo, Phys. Rev. Lett. **63**, 1845 (1989).
[24] D. Z. Chi, R. T. P. Lee, S. J. Chua, S. J. Lee, S. Ashok, and D.-L. Kwong, J. Appl. Phys. **97**, 113706 (2005).
[25] E. Simoen, K. Opsomer, C. Claeys, K. Maex, C. Detavernier, R. L. V. Meirhaeghe, and P. Clauws, J. Appl. Phys. **104**, 023705 (2008).
[26] S. Gaudet, C. Detavernier, A. J. Kellock, P. Desjardins, and C. Lavoie, J. Vac. Sci. Technol. A **24**, 474 (2006).
[27] D. P. Brunco, B. D. Jaeger, G. Eneman, J. Mitard, G. Hellings, A. Satta, V. Terzieva, L. Souriau, F. E. Leys, G. Pourtois, M. Houssa, G. Winderickx, E. Vrancken, S. Sioncke, K. Opsomer, G. Nicholas, M. Caymax, A. Stesmans, J. V. Steenbergen, P. W. Mertens, M. Meuris, and M. M. Heyns, J. Electrochem. Soc. **155**, H552 (2008).
[28] K. Prabhakaran and T. Ogino, Appl. Surf. Sci. **100**, 518 (1996).
[29] C. Zeng, W. Zhu, S. C. Erwin, Z. Zhang, and H. H. Weitering, Phys. Rev. B **70**, 205340 (2004).
[30] A. P. Li, J. F. Wendelken, J. Shen, L. C. Feldman, J. R. Thompson, and H. H. Weitering, Phys. Rev. B **72**, 195205 (2005).
[31] P. D. Padova, J.-M. Mariot, L. Favre, I. Berbezier, B. Olivieri, P. Perfetti, C. Quaresima, C. Ottaviani, A. Taleb-Ibrahimi, P. L. Fevre, F. Bertran, O. Heckmann, M. Richter, W. Ndiaye, F. D'Orazio, F. Lucari, C. Cacho, and K. Hricovini, Surf. Sci. **605**, 638 (2011).
[32] W. C. Fan and A. Ignatiev, Phys. Rev. B **40**, 5479 (1989).
[33] S.-J. Tang, T. Miller, and T.-C. Chiang, Phys. Rev. Lett. **96**, 036802 (2006).

[34]S.-J. Tang, W.-K. Chang, Y.-M. Chiu, H.-Y. Chen, C.-M. Cheng, K.-D. Tsuei, T. Miller, and T.-C. Chiang, Phys. Rev. B **78**, 245407 (2008).
[35]Y. Liu, N. J. Speer, S.-J. Tang, T. Miller, and T.-C. Chiang, Phys. Rev. B **78**, 035443 (2008).
[36]F. Krok, F. Buatier de Mongeot, M. Goryl, J. J. Kolodziej, and M. Szymonski, Phys. Rev. B **81**, 235414 (2010).
[37]D. Dornisch, W. Moritz, H. Schulz, R. Feidenhans'l, M. Nielsen, F. Grey, R. Johnson, and G. L. Lay, Surf. Sci. **274**, 215 (1992).
[38]M. Hammar, M. Göthelid, U. O. Karlsson, and S. A. Flodström, Phys. Rev. B **47**, 15669 (1993).
[39]H. Huang, H. Over, S. Y. Tong, J. Quinn, and F. Jona, Phys. Rev. B **49**, 13483 (1994).
[40]M. Göthelid, M. Hammar, U. O. Karlsson, C. Wigren, and G. LeLay, Phys. Rev. B **52**, 14104 (1995).
[41]J. S. Tsay, H. Y. Nieh, C. S. Yang, Y. D. Yao, and T. S. Chin, J. Appl. Phys. **93**, 8728 (2003).
[42]J. S. Tsay, H. Y. Nieh, Y. D. Yao, and T. S. Chin, J. Magn. Magn. Mater. **282**, 78 (2004).
[43]G. A. Smith, L. Luo, S. Hashimoto, W. M. Gibson, and N. Lewis, J. Vac. Sci. Technol. A **7**, 1475 (1989).
[44]T.-Y. Fu, C.-L. Lin, and S.-L. Tsay, Surf. Sci. **600**, 4058 (2006).
[45]T.-Y. Fu, S.-L. Tsay, and C.-L. Lin, J. Nanosci. Nanotechnol. **8**, 608 (2008).
[46]S.-L. Tsay, C.-Y. Kuo, C.-L. Lin, W.-C. Chen, and T.-Y. Fu, Surf. Interface Anal. **40**, 1641 (2008).
[47]C.-L. Lin, S.-L. Tsay, C.-R. Chen, X.-L. Huang, and T.-Y. Fu, J. Nanosci. Nanotechnol. **10**, 4500 (2010).
[48]X.-L. Huang, A. Tomaszewska, C.-H. Chou, C.-Y. Hsu, C.-L. Lin, and T.-Y. Fu, J. Nanopart. Res. **14**, 1257 (2012).
[49]K. Schouteden, E. Lijnen, D. A. Muzychenko, A. Ceulemans, L. F. Chibotaru, P. Lievens, and C. Van Haesendonck, Nanotechnology **20**, 395401 (2009).
[50]K. Schouteden, D. A. Muzychenko, P. Lievens, and C. Van Haesendonck, J. Nanosci. Nanotechnol. **9**, 6767 (2009).
[51]I. Horcas, R. Fernandez, J. M. Gomez-Rodriguez, J. Colchero, J. Gomez-Herrero, and A. M. Baro, Rev. Sci. Instrum. **78**, 013705 (2007).
[52]A. I. Oreshkin, D. A. Muzychenko, I. V. Radchenko, V. N. Mancevich, V. I. Panov, and S. I. Oreshkina, Rev. Sci. Instrum. **77**, 116116 (2006).
[53]D. J. Chadi and C. Chiang, Phys. Rev. B **23**, 1843 (1981).
[54]R. S. Becker, J. A. Golovchenko, and B. S. Swartzentruber, Phys. Rev. Lett. **54**, 2678 (1985).
[55]R. S. Becker, B. S. Swartzentruber, J. S. Vickers, and T. Klitsner, Phys. Rev. B **39**, 1633 (1989).
[56]E. S. Hirschorn, D. S. Lin, F. M. Leibsle, A. Samsavar, and T.-C. Chiang, Phys. Rev. B **44**, 1403 (1991).
[57]R. Feenstra and A. Slavin, Surf. Sci. **251-252**, 401 (1991).
[58]N. Takeuchi, A. Selloni, and E. Tosatti, Phys. Rev. Lett. **69**, 648 (1992).
[59]R. M. Feenstra, G. Meyer, F. Moresco, and K. H. Rieder, Phys. Rev. B **64**, 081306 (2001).
[60]R. M. Feenstra, S. Gaan, G. Meyer, and K. H. Rieder, Phys. Rev. B **71**, 125316 (2005).
[61]I. Razado-Colambo, J. He, H. M. Zhang, G. V. Hansson, and R. I. G. Uhrberg, Phys. Rev. B **79**, 205410 (2009).
[62]C.-L. Lin, S.-L. Tsay, C.-R. Chen, X.-L. Huang, and T.-Y. Fu, J. Surf. Sci. Nanotechnol. **7**, 521 (2009).
[63]X.-L. Huang, C.-H. Chou, C.-L. Lin, A. Tomaszewska, and T.-Y. Fu, Thin Solid Films **519**, 8410 (2011).
[64]R. M. Feenstra, J. Y. Lee, M. H. Kang, G. Meyer, and K. H. Rieder, Phys. Rev. B **73**, 035310 (2006).
[65]R. D. Bringans and H. Höchst, Phys. Rev. B **25**, 1081 (1982).
[66]T. Yokotsuka, S. Kono, S. Suzuki, and T. Sagawa, J. Phys. Soc. Jpn. **53**, 696 (1984).
[67]J. M. Nicholls, G. V. Hansson, R. I. G. Uhrberg, and S. A. Flodström, Phys. Rev. B **33**, 5555 (1986).
[68]J. Aarts, A. J. Hoeven, and P. K. Larsen, Phys. Rev. B **37**, 8190 (1988).
[69]F. J. Himpsel, Surf. Sci. Rep. **12**, 3 (1990).
[70]J. A. Stroscio and R. M. Feenstra, Methods Exp. Phys. **27**, 95 (1993), http://www.sciencedirect.com/science/article/pii/S0076695X08600095.
[71]P. Hohenberg and W. Kohn, Phys. Rev. **136**, B864 (1964).
[72]W. Kohn and L. J. Sham, Phys. Rev. **140**, A1133 (1965).
[73]J. P. Perdew, K. Burke, and M. Ernzerhof, Phys. Rev. Lett. **77**, 3865 (1996).
[74]J. P. Perdew and Y. Wang, Phys. Rev. B **33**, 8800 (1986).
[75]P. Ordejón, E. Artacho, and J. M. Soler, Phys. Rev. B **53**, R10441 (1996).
[76]J. M. Soler, E. Artacho, J. D. Gale, A. García, J. Junquera, P. Ordejón, and D. Sánchez-Portal, J. Phys.: Condens. Matter **14**, 2745 (2002).
[77]N. Troullier and J. L. Martins, Phys. Rev. B **43**, 1993 (1991).
[78]H. J. Monkhorst and J. D. Pack, Phys. Rev. B **13**, 5188 (1976).
[79]R. D. Meade and D. Vanderbilt, Phys. Rev. B **40**, 3905 (1989).
[80]D. A. Muzychenko, K. Schouteden, M. Houssa, S. V. Savinov, and C. Van Haesendonck, Phys. Rev. B **85**, 125412 (2012).
[81]D. A. Muzychenko, K. Schouteden, V. I. Panov, and C. Van Haesendonck, Nanotechnology **23**, 435605 (2012).
[82]N. Takeuchi, A. Selloni, and E. Tosatti, Phys. Rev. B **51**, 10844 (1995).
[83]J. Tersoff and D. R. Hamann, Phys. Rev. Lett. **50**, 1998 (1983).
[84]J. Tersoff and D. R. Hamann, Phys. Rev. B **31**, 805 (1985).
[85]M. Rohlfing, R. Temirov, and F. S. Tautz, Phys. Rev. B **76**, 115421 (2007).
[86]R. M. Feenstra, G. Meyer, and K. H. Rieder, Phys. Rev. B **69**, 081309 (2004).
[87]R. Hoffmann, J. Phys.: Condens. Matter **5**, A1 (1993).
[88]R. Dronskowski and P. E. Bloechl, J. Phys. Chem. **97**, 8617 (1993).
[89]G. Bester and M. Fähnle, J. Phys.: Condens. Matter **13**, 11541 (2001).
[90]V. Paul-Boncour and S. F. Matar, Phys. Rev. B **70**, 184435 (2004).
[91]R. S. Mulliken, J. Chem. Phys. **23**, 1833 (1955).
[92]H. P. Sun, Y. B. Chen, X. Q. Pan, D. Z. Chi, R. Nath, and Y. L. Foo, Appl. Phys. Lett. **87**, 211909 (2005).
[93]V. G. Myagkov, Y. L. Mikhlin, L. E. Bykova, G. N. Bondarenko, and I. A. Turpanov, Dokl. Phys. Chem. **431**, 72 (2010).